HHS Public Access

Author manuscript

Glia. Author manuscript; available in PMC 2019 July 22.

Published in final edited form as:

Glia. 2018 December ; 66(12): 2700–2718. doi:10.1002/glia.23522.

Inhibition of hematopoietic cell kinase dysregulates microglial function and accelerates early stage Alzheimer's disease-like neuropathology

Siok Lam Lim[1,2], **Diana Nguyen Tran**[2], **Joannee Zumkehr**[1,2], **Christine Chen**[2], **Sagar Ghiaar**[2], **Zanett Kieu**[2], **Emmanuel Villanueva**[2], **Victoria Gallup**[2], **Carlos J. Rodriguez-Ortiz**[1,2], **Masashi Kitazawa**[1,2,*]

[1]Center for Occupational and Environmental Health, Department of Medicine, University of California, Irvine, CA 92617, USA

[2]Molecular and Cell Biology, University of California, Merced, CA 95340, USA

Abstract

Emerging evidence have posited that dysregulated microglia impair clearance and containment of amyloid-β (Aβ) species in the brain, resulting in aberrant buildup of Aβ and onset of Alzheimer's disease (AD). Hematopoietic cell kinase (Hck) is one of the key regulators of phagocytosis among the Src family tyrosine kinases (SFKs) in myeloid cells, and its expression is found to be significantly altered in AD brains. However, the role of Hck signaling in AD pathogenesis is unknown. We employed pharmacological inhibition and genetic ablation of Hck in BV2 microglial cells and J20 mouse model of AD, respectively, to evaluate the impact of Hck deficiency on Aβ-stimulated microglial phagocytosis, Aβ clearance and resultant AD-like neuropathology. Our *in vitro* data reveal that pharmacological inhibition of SFKs/Hck in BV2 cells and genetic ablation of their downstream kinase, spleen tyrosine kinase (Syk), in primary microglia significantly attenuate Aβ oligomers-stimulated microglial phagocytosis. Whereas in Hck-deficient J20 mice, we observed exacerbated Aβ plaque burden, reduced microglial coverage, containment and phagocytosis of Aβ plaques, and induced iNOS expression in plaque-associated microglial clusters. These multifactorial changes in microglial activities led to attenuated PSD95 levels in hippocampal DG and CA3 regions, but did not alter the post-synaptic dendritic spine morphology at the CA1 region nor cognition function of the mice. Hck inhibition thus accelerates early stage AD-like neuropathology by dysregulating microglial function and inducing neuroinflammation.

[*]**Corresponding author:** Masashi Kitazawa, Ph.D., Associate Professor, Center for Occupational and Environmental Health, Department of Medicine, University of California, Irvine, 100 Theory Dr., Suite 100, Irvine, CA 92617, 949-824-1255, kitazawa@uci.edu.

AUTHORSHIPS

All *in vitro* studies, ELISA, protein extraction and western blot analysis, RNA extraction and real-time PCR analysis, dendritic spine analysis and statistical analyses were conducted by SLL. Guidance on 7PA2-CM generation, microdissection, ELISA and immunostaining were provided by JZ. Animal husbandry and genotyping were done by SLL, DNT, ZK, EV, CC, VG and SG, and tissue collection were conducted by SLL, DNT, CC, ZK, JZ and CJRO. Behavioral tests were designed by CJRO and executed by CJRO and SLL. NOR and OIP scoring were done by EV and VG. Tissue sectioning was done by DNT, CC and SG, while immunostaining and analyses were done by SLL, DNT and CC. Experiments were conceived and designed by MK and SLL. Manuscript was written by SLL and critically reviewed by MK. All authors read and approved the final manuscript.

CONFLICT OF INTEREST STATEMENT

The authors declare that they have no competing interests.

Our data implicate that Hck pathway plays a prominent role in regulating microglial neuroprotective function during the early stage of AD development.

Keywords

Microglia; Alzheimer's disease; Hematopoietic cell kinase; Spleen tyrosine kinase; amyloid-β, BV2 cells; J20 mice

1 INTRODUCTION

Recent studies strongly support that accelerated buildup of amyloid-beta (Aβ) in the brain is primarily mediated by an impairment of Aβ clearance, rather than the overproduction of Aβ in Alzheimer's disease (AD) (Mawuenyega et al., 2010; Querfurth & LaFerla, 2010; Tarasoff-Conway et al., 2015; Wildsmith, Holley, Savage, Skerrett, & Landreth, 2013). Microglia, the resident immune cells in the brain, are believed to play a key role in removing Aβ species and regulating neuroinflammation (Cunningham, 2013; Eikelenboom et al., 2002; Malm, Jay, & Landreth, 2015). Our previous studies have shown that inhibiting microglial phagocytosis and activating pro-inflammatory responses exacerbate AD neuropathology (Kitazawa et al., 2011) while stimulating microglial phagocytosis clears Aβ and rescues cognition (Dunn et al., 2015; Medeiros et al., 2013). It is thus evident that functional inactivation of microglia significantly impair its ability to clear Aβ, leading to a pathological buildup of Aβ and the onset of AD (Lim, Rodriguez-Ortiz, & Kitazawa, 2015). In support of this notion, a recent longitudinal human study reveals an early protective peak and a late pro-inflammatory peak of microglial activation in the pathogenesis of AD (Fan, Brooks, Okello, & Edison, 2017). Hence, identifying molecules or signaling pathways that mediate microglial dysregulation in the pathogenesis of AD is a key to retard or halt the progression of the disease (Wes, Sayed, Bard, & Gan, 2016).

A plethora of evidence have shown that *in vitro* and *in vivo* Aβ stimulation of microglia augments tyrosine phosphorylation (Dhawan & Combs, 2012; Dhawan, Floden, & Combs, 2012), which correlates with elevated levels of microglial phospho-tyrosine and phospho-Src in AD brains (Dhawan et al., 2012; Wood & Zinsmeister, 1991). Hematopoietic cell kinase (Hck) is a member of the Src family tyrosine kinases (SFKs) which mediate immunoreceptor-induced phagocytic activation in microglia (Choucair et al., 2006; Linnartz & Neumann, 2013), while spleen tyrosine kinase (Syk) is a non-receptor tyrosine kinase acting downstream of SFKs (Lowell, 2011). Integrative network-based approach analyzing 1,647 post-mortem brain tissues of AD patients and non-demented subjects identified eight common causal regulators for all immune networks, and Hck was ranked third after TYROBP (DAP12) and DOCK2, based on combined ranking score of regulatory strength and differential expression in AD brains (Zhang et al., 2013).

SFKs mediate Aβ-stimulated microglial phagocytosis (Koenigsknecht & Landreth, 2004), and Hck is the key regulator of phagocytosis in myeloid cells among the SFKs (Guiet et al., 2008; Lowell, Soriano, & Varmus, 1994). However, there is no direct study on the effect of Hck regulation on Aβ-stimulated microglial phagocytosis to date. We hypothesize that inactivation of Hck and Syk impairs microglial phagocytosis and Aβ clearance, leading to

the development of AD neuropathology and cognitive decline. To test our hypothesis, we conducted *in vitro* inhibition of SFKs/Hck in BV2 microglial cells, genetic ablation of Syk in primary microglia, and *in vivo* ablation of Hck in J20 mouse model of AD to evaluate the impact of Hck deficiency on Aβ-stimulated microglial phagocytosis, Aβ clearance and resultant AD-like neuropathology. This study will be the first that evaluates the deficiency of Hck in AD-like pathology, thereby providing knowledge for therapeutic interventions for treating AD.

2 MATERIALS AND METHODS

2.1 7PA2, CHO and primary microglial cell culture

7PA2 cells are transfected Chinese hamster ovary (CHO) cells that express V717F AD mutation in amyloid-β precursor protein 751 ($A\beta PP_{751}$) (Walsh et al., 2002). Upon cell confluent, 7PA2 cells secrete Aβ monomers and oligomers naturally in the conditioned medium (CM). Both 7PA2 and control CHO cells were kindly contributed by Dr. Edward Koo (University of California, San Diego), and were grown in Dulbecco's Modified Eagle's medium (DMEM) supplemented with 10% fetal bovine serum (FBS), 50 units penicillin, and 50 μg streptomycin (Thermo Fisher Scientific Inc.). When cells were near confluent, they were washed once with serum free medium (SFM) and replaced with fresh stock of the same medium. Cells were then incubated for ~16 h, and the CM was collected and centrifuged at 1000*g* for 10 mins at 4°C to remove cell debris. CM were then stored at −80°C until $A\beta_{40}$ and $A\beta_{42}$ quantification using ELISA as described in Section 2.8. 7PA2-CM with substantiate expression of $A\beta_{40}$ (352–570 pM) and $A\beta_{42}$ (320–480 pM), but negligible levels of the same proteins in CHO-CM were applied to BV2 cells and primary microglia for phagocytosis assay and to BV2 cells for biochemical analysis.

Primary microglia were isolated from Syk/Cre double homozygous mice on postnatal day 0–3. Syk/Cre mice were generated by crossing Syk-floxed (#017309 from the Jackson Laboratory) and Rosa Cre-ERT2 mice (#008463 from the Jackson Laboratory) to allow *in vitro* 4-hydroxytamoxifen (4-OHT, Sigma-Aldrich Corporation)-inducible deletion of Syk (Ozaki et al., 2012). Extraction of primary microglia was done as described (Tanaka, Murakami, Bando, & Yoshida, 2015) with some modifications. Briefly, mouse brains were collected in culture medium as described above and microdissected to remove olfactory bulb, cerebellum and meninges. Thereafter, the brain tissues were triturated with micropipette tips, digested in 0.05% Trypsin-EDTA for 15 mins at 37 °C and filtered through 70 μm nylon cell strainer (BD Falcon). Cell suspension from 6–9 pups were combined and cultured in one T-75 flask, and after an overnight incubation, cells were replenished with fresh medium and allowed to grow for 7–10 days without changing medium. Microglial cells growing on top of the astrocytes monolayers were isolated by shaking the culture flask.

2.2 *In vitro* phagocytosis assay and biochemical analysis

BV2 cells are immortalized murine microglial/macrophage cells that elicit robust phagocytic activity upon stimulation (Kopec & Carroll, 1998). The BV2 cells used in this assay were kindly provided by Dr. Gary Landreth (Case Western Reserve University). Cells were

cultured in DMEM supplemented with 5% FBS, 50 units penicillin, and 50 μg streptomycin. *In vitro* phagocytosis assay was conducted as established by several groups (Koenigsknecht-Talboo & Landreth, 2005; Koenigsknecht & Landreth, 2004; Pan et al., 2011; Song, Zhou, & Chen, 2012) with some modifications. BV2 cells were seeded at 5×10^4 cells/well on poly-D-lysine coated cover slips placed in 24 well plate. When the cells reached ~60% confluence, they were washed once with SFM and incubated with fresh SFM for another 3 h. Cells were then treated with either SFM, 10 μM pan-Src inhibitor (PP2; Sigma-Aldrich Corporation) or 1 μM Syk-specific inhibitor (BAY 61–3606; Sigma-Aldrich Corporation) for 30 min. Thereafter, 1 mg/ml mouse complement-opsonized zymosan (mOZ, prepared as described in Koenigsknecht & Landreth, 2004), 1 μg/ml lipopolysaccharide (LPS; Sigma-Aldrich Corporation), 7PA2- or CHO-CM were added to the cells, in the presence of either SFM or inhibitors, and incubated for another 1 hr. At the last 30 mins of incubation, 2×10^7 Nile Red FluoSpheres Carboxylate-Modified Microspheres (Invitrogen) were added to each well as marker of phagocytosis. Cells were finally rinsed three times with phosphate buffered saline (PBS), fixed with 4% paraformaldehyde (PFA), and immunostained with Alexa Fluor 488 Phalloidin (Life Technologies Corporation) and DAPI (Invitrogen) to label cellular cytoskeleton and nuclei, respectively. Three representative fluorescent images from each well were taken with EVOS FL Cell Imaging System (Thermo Fisher Scientific Inc.) using a 20x objective. Number of microspheres phagocytosed by each cell were counted manually using the Cell Counter plugins on ImageJ software (National Institute of Health) and expressed as phagocytic efficiency (%) and % phagocytic cells as described (Koenigsknecht & Landreth, 2004). To determine phagocytic efficiency (%), points were assigned according to the number of microspheres per cell wherein one point was given for a cell phagocytosing one microsphere, two points for two microspheres, and so on, up to a maximum of six points for more than five microspheres phagocytosing per cell. Number of cells containing x microspheres in the image was next multiplied by the point value. Each of these values were then added together and divided by the total number of cells counted. To express in terms of % phagocytic cells, number of cells phagocytosing one or more microspheres were taken relative to the total number of cells counted in the image. Averaged value from the three images per well thus represented one data value and was compared with that of other treatments in replicates.

To assess the signaling pathways mediating ligand-stimulated BV2 cells phagocytosis, cells were plated at 5×10^5 cells/well on 6 well plate to achieve 80% confluency by the following day. Cells were rinsed once with SFM before incubated in fresh SFM for another 3 h. Cells were then treated with either SFM or 10 μM PP2 for 30 min. Thereafter, cells were replenished with either SFM (control), mOZ (1 mg/ml), 7PA2- or CHO-CM, and incubated for 60 min. For wells that were previously treated with PP2, they were replenished with mOZ or 7PA2-CM spiked with PP2. At the end of the incubation, cells were washed twice with PBS and lysed in 70 μl of M-PER Mammalian Protein Extraction Reagent (Thermo Fisher Scientific Inc.) complemented with Halt protease and phosphatase inhibitors (Thermo Fisher Scientific Inc.). The cell lysates were then centrifuged at 14,000 rpm for 20 min at 4 °C to collect protein lysate devoid of cellular debris.

To conduct biochemical analysis of the signaling proteins, protein concentration from BV2 cellular protein lysates were measured using the Bradford protein assay (Bio-Rad

Laboratories), and standardized protein mass were analyzed as described under Section 2.7. Primary antibodies used in this experiment were phospho-Syk (Tyr525/526) (pSyk; Cell Signaling), Syk (N-19) (Santa Cruz Biotechnology, Inc.), YM1 (STEMCELL Technologies), inducible nitric oxide synthase (iNOS) (BD Transduction Laboratories), and tubulin (Sigma-Aldrich Corporation).

Primary microglial phagocytosis assay was conducted as described for BV2 cells with some modifications. Primary microglia were seeded at 60×10^3 cells/well on CC2™ Chamber Slide System (Thermo Fisher Scientific Inc.) and incubated for 30 min in culture medium before washing twice with PBS to remove oligodendrocytes precursor cells. Primary microglia were then cultured overnight in mixed glia-CM before treating some of the cells with 0.6 μM 4-OHT for four days, followed by culture medium for one day, to knockdown Syk. On day six, cells were prepared for *in vitro* phagocytosis assay as described above, using mOZ (1 mg/ml), 7PA2- or CHO-CM as stimuli.

2.3 Animals

Hck-knocked out (Hck-KO) mice were generously provided by Dr. Clifford Lowell (University of California, San Francisco). Hemizygous PDGF-$hAPP_{Sw,Ind}$ J20 mice and wild-type (WT) mice were purchased from Jackson Laboratory. Hck-deficient J20 (J20/Hck-KO) mice was generated by crossing J20 mice with Hck-KO mice. All mice were of C57BL/6 background and both genders were used in this study. Mice were analyzed at 5–8 months old when they are at an early stage of pathological development. All animal studies performed were approved by the University of California Institutional Animal Care and Use Committee and were in accordance with Federal guidelines.

2.4 Tissue collection

Littermates of J20 and WT mice, as well as Hck-KO and J20/Hck-KO mice were euthanized at 6–8 months old after behavioral studies at 5–6 months of age. Mice were perfused with ice-cold PBS and the brains were collected in one of the three ways as followed: i) for immunostaining, the hemibrain was fixed with 4% PFA; ii) for dendritic spine analysis, the hemibrain was immersed in Golgi solution; iii) for biochemical analyses, the hemibrain was microdissected into hippocampus and cortex, and frozen at −80°C until further processing.

2.5 Immunohistochemical analysis

Hemibrains designated for immunostaining were cryopreserved in −80°C after fixing in 4% PFA and cryoprotected in 30% sucrose for 2–3 days each. Thereafter, hemibrains were sectioned coronally at 20 μm using a freezing microtome (SM2010R; Leica Biosystems) and sections were stored in PBS with 0.05% sodium azide at 4°C. Sections from different mice at bregma position −2.54 mm (according to the mouse brain atlas of Franklin and Paxinos, Third Edition, 2007) were then mounted on microscopic slides and processed under the same conditions. Negative control slides were prepared by omitting primary antibodies to check for non-specific labeling.

To assess for Aβ plaque burden, two additional sections (± 10 sections from bregma −2.54 mm) per mouse were pretreated with 90% formic acid for 5 mins as modified from

previously reported protocols (Kitazawa et al., 2011; Medeiros et al., 2011), before incubated in Aβ plaque antibodies: 6E10 or 4G8 (Covance Inc.). To reduce non-specific staining of 6E10 antibody, sections were pretreated with Mouse on Mouse (M.O.M™) Detection Kit (Vector Laboratories) according to the kit's instructions. Aβ plaques were then visualized using either colorimetric method or immunofluorescence method which allows double or triple-labeling of other proteins on the same section. For colorimetric method, ABC Peroxidase Standard Staining Kit (Thermo Fisher Scientific Inc.) and DAB Peroxidase Substrate Kit (Vector Laboratories) were applied on the sections and labeled plaques were imaged on EVOS XL Core Imaging System (Thermo Fisher Scientific Inc.). For immunofluorescent labeling of primary antibodies, Alexa Fluor 488, 555 or 633 conjugated secondary antibodies (Life Technologies Corporation) raised in corresponding species were applied to the sections. All sections were also stained with DAPI for nuclear labeling. Fluorescent images were taken with either BZ-9000 All-in-one Fluorescence Microscope (KEYENCE Corp. of America) or confocal laser microscope (DM2500; Leica Microsystems) when volumetric analysis was required. For Aβ plaque burden analysis, plaques were imaged in hippocampus, cortex near CA1 and CA3 regions, entorhinal cortex and amygdala. Plaque areas were quantified using ImageJ software, and plaque burden was calculated by taking % of plaque areas over the entire area of the image field.

To label Thioflavin-S plaques, sections were stained for 10 min in 0.5% Thioflavin-S (Sigma-Aldrich Corporation) in 50% ethanol (in the dark) without formic acid treatment. Thioflavin-S plaques of ≥ 30 μm were captured with confocal microscope using a 40x objective with 2x zoom in 1 μm z-separation step. To assess for microglial activities around the plaques, Iba-1 (Wako Laboratory Chemicals), and CD45 and CD11b (AbD Serotec) primary antibodies were used, and were quantified at within 20 μm from the edge of the plaque of diameter ≥ 30 μm, including the area of the plaque itself (Ulrich et al., 2014). CD68 (AbD Serotec) primary antibody was applied to assess the activation of phagolysosomes in microglial cells after Aβ phagocytosis. pSyk (Tyr525/526) and iNOS antibodies were also used to assess activation of Syk and pro-inflammatory state of microglia clustering around plaques, respectively. Area covered by respective proteins were measured using ImageJ, while volumetric image measurements, microglial number and morphology were made using Imaris software (Bitplane Inc.) as previously described (Marsh et al., 2016). Plaque sphericity was quantified using the Imaris software to assess the diffusivity of plaques. To determine Aβ internalization ratio, volume of Aβ found within $CD68^+$ phagolysosomes in $Iba1^+$ microglia was normalized to microglial number on the plaque and Aβ plaque volume within the field (Marsh et al., 2016).

To label synaptic proteins, synaptophysin (Abcam) and PSD95 (NeuroMab) antibodies were applied, and protein intensities in the DG, CA1 and CA3 regions of the hippocampus were quantified. Using a 20x objective on the EVOS FL Cell Imaging System as previously described (Zumkehr et al., 2015), three different areas in the DG, and two of each in the CA1 and CA3 regions were imaged. In each image, five 50 × 50 pixel area were selected from the four corners and the middle of the image that best represent the protein intensity of the region and were quantified using ImageJ. An average of all areas from each region was calculated and represented the synaptic protein intensities in the DG, CA1 and CA3 regions of the hippocampus. Data are expressed as % synaptic protein intensities per genotype

relative to that of Hck-KO mice as the tissues were sectioned in two batches that they labeled with the antibodies differently. Both batches of tissues consisted of Hck-KO mice as a normalizing control.

2.6 Dendritic spine analysis

Hemibrains designated for dendritic spine analysis were treated with Hito Golgi-Cox OptimStain Kit (Hitobiotec Inc.), embedded in tissue freezing medium (O.C.T, Fisher Scientific) and sectioned at 80 μm with cryostat (Leica Biosystems). Golgi-stained sections were mounted on gelatin-coated microscopic slides, and dendritic spines were assessed using Neurolucida software (MBF Bioscience). To represent the entire anteroposterior extent of the hippocampus, every four sections between bregma −1.46 mm anterior and −3.40 mm posterior were chosen for analysis. In each of the selected sections, five dendritic segments were traced on five different pyramidal neurons at the stratum radiatum (SR) of hippocampal CA1 region as previously described (Beauquis et al., 2014; Pujadas et al., 2014). Following these criteria, dendritic spines from 25–35 pyramidal neurons were analyzed for each mouse. The length of dendrites traced and the types of spines identified on the traced dendrites were determined by the software for statistical analysis.

2.7 Protein extraction and western blot analysis

Protein was extracted from hippocampus by homogenizing in T-PER Tissue Protein Extraction Reagent (Thermo Fisher Scientific Inc.) complemented with protease and phosphatase inhibitors (Sigma-Aldrich Corporation), followed by centrifugation at 100,000*g* for 1 h at 4 °C to get detergent-soluble fraction and –insoluble pellet. Pellet was further homogenized in 70% formic acid and centrifuged as before to collect detergent-insoluble fraction. All protein fractions were stored at −80°C until further analysis.

Protein concentration from hippocampus in detergent-soluble fractions were measured using the Bradford protein assay. Standardized protein mass were separated by SDS-PAGE and transferred to Immobilon-FL PVDF membrane (EMD Millipore). Membranes were blocked in Odyssey Blocking Buffer (LI-COR Biosciences) for 1 h at room temperature, before immunoblotted overnight with shaking at 4°C with the following antibodies diluted in Odyssey Blocking Buffer with 0.2% Tween 20 (Thermo Fisher Scientific Inc.): 6E10 (Covance Inc.), CT20 and beta-site amyloid precursor protein cleaving enzyme 1 (BACE1) (Calbiochem), YM1, arginase-1 (Arg1; Santa Cruz Biotechnology, Inc.) or tubulin. Membranes were then washed in TBST, before incubated with corresponding IRDye secondary antibodies (LI-COR Biosciences) diluted in TBST/SDS and 5% fat-free milk for 1 h at room temperature. Membranes were washed in TBST thereafter and scanned using Odyssey Imaging System (LI-COR Biosciences). Band intensities were quantified with Image Studio software (version 5.2, LI-COR Biosciences) and normalized to that of tubulin which serves as protein loading control.

2.8 Quantitative analysis of Aβ by enzyme-linked immunosorbent assay (ELISA)

$A\beta_{40}$ and $A\beta_{42}$ were quantified in both detergent-soluble and –insoluble fractions, as well as in 7PA2- and CHO-CM by ELISA as described previously (Zumkehr et al., 2015).

2.9 RNA isolation and real-time polymerase chain reaction (PCR)

Total RNA was isolated separately from the hippocampus and cortex of the mice using Direct-zol RNA MiniPrep (ZYMO Research). RNA purity and concentration were assessed using NanoDrop spectrophotometer, and 1 μg of total RNA was reversed-transcribed to cDNA using iScript cDNA Synthesis kit (Bio-Rad Laboratories). 1 ul of the synthesized cDNA was then amplified via real-time PCR using iTaq Universal SYBR Green Supermix (Bio-Rad Laboratories) on the CFX Connect Real-time system (Bio-Rad Laboratories). Sequences of the mouse primers used were as followed: Gapdh-F (forward) 5'-GAAGCCCATCACCATCTTCCA-3', Gapdh-R (reverse) 5'-TTGGCTCCACCCTTCAAGTG-3', Arg1-F 5'-CAGTGGCTTTAACCTTGGCT-3', Arg1-R 5'-GTCAGTCCCTGGCTTATGGT-3', Fizz1-F 5'-CTGCTACTGGGTGTGCTTGT-3', Fizz1-R 5'-GGCAGTTGCAAGTATCTCCA-3', Ym1-F 5'-TCTATGCCTTTGCTGGAATG-3', Ym1-R 5'-CAGGTCCAAACTTCCATCCT-3'. Parameters of the real-time PCR cycles were 95°C for 10 min for initial denaturing, 95°C for 30 s for denaturing, 60°C for 1 min for annealing, and 72°C for 1 min for extension. The last 3 parameters were repeated for 35 times before the melt curves were generated. Quantification cycle (Cq) values and melt curves were determined by Bio-Rad Laboratories CFX Manager 3.1. Relative mRNA levels were calculated by the $2^{-\Delta\Delta Ct}$ method (Livak & Schmittgen, 2001) using Gapdh as the reference gene and genes expressed by WT mice as the calibrators.

2.10 Novel Object Recognition (NOR)

NOR was conducted as previously described (Rodriguez-Ortiz et al., 2013) with some modifications. Mice were first habituated to the trainer by handling them for 2 mins each in three consecutive days. The mice handling was then extended to another 5 mins of habituation to a Plexiglas arena without objects. After five consecutive days of habituation (day nine of the training), mice were habituated to the training room for 15 mins before task training and 2 h after (for memory retention). Mice were trained by exposing them to two identical objects placed side-by-side in the arena for 10 mins. At 2 h later, mice were allowed to explore one familiar object (ie. object exposed before) and one novel (new) object in the arena for 5 mins. Mice activities in the arena were recorded using video camera, which was later replayed to determine their exploration behaviors and quantified as recognition index. Recognition index (RI) indicates the relative time mouse spent in exploring the novel object, and significance from RI of 0.5 (chance level) using one sample *t* test denotes novel object recognition. Exploration was considered when mouse pointed its head towards an object at a distance of < 2.5 cm with its neck extended and vibrissae moving. Simple proximity, chewing and sitting on objects were not considered as exploratory behaviors. Mice that did not explore both objects during training were not used for behavioral analysis. Objects used in this task were carefully selected to prevent preference or phobic behaviors. To eliminate olfactory cues, the objects and arena were thoroughly cleaned with 70% ethanol and the beddings were removed of droppings and stirred between mice.

2.11 Object In Place (OIP)

OIP training was conducted on the day after NOR test, with similar procedures except for the set of objects used and the object placement. During task training, a new set of identical objects were placed side-by-side in the arena for mice to explore for 10 mins. 2 h later, mice were exposed to the same set of identical objects, with one of the objects moved to either the left or right side of the arena. RI for OIP indicates the relative time mouse spent in exploring the object at the novel place.

2.12 Morris Water Maze (MWM)

MWM was conducted as described previously (Rodriguez-Ortiz et al., 2013) with some modifications. Mice were trained to locate a circular and transparent Plexiglas platform submerged at 1 cm beneath the surface of the water, which was invisible to them when they were swimming in the 1 m diameter water tank. The platform was placed in an equidistant position in a quadrant of the circular tank, and visual cues were placed on three sides of the wall for spatial reference. Mice were subjected to six training trials per day for three consecutive days whereby WT mice of 5–6 months old reached the training criterion of 25 s in escape latency by the third day of training. On the first two days of training, mice were placed on the platform for 30 s, and allowed to rest for 30 s in a dry cage. Trials involved placing the mice into the tank at one of the four designated starting points in a pseudorandom order. Mice were given up to 60 s to swim to the platform. If they failed to do so, they were be manually guided to the platform. Once on the platform, they were left there for another 30 s, before being transferred to a dry cage to rest for 30 s. On Day three of the training, mice were placed directly into the tank without prior placement on the platform. At 72 h after the last training, the platform was removed and mice were tested by placing in the tank at the quadrant opposite of where the platform was supposed to be. At 60 s, mice were removed from the tank and allowed to rest for 30 s. Mice were next returned to the tank at the same location, but with the platform in the place this round. At one week after the last training, mice were again tested with platform removed from the tank. All MWM trainings and tests were recorded by video camera and analyzed using VideoTrack system (ViewPoint Behavior Technology). Behavioral performance was quantified in terms of escape latency (time taken to reach area occupied by platform during training), number of platform crosses (number of times mouse crosses the platform area during the 60 s), and % time spent in the target (with platform) and opposite (from platform) quadrants.

2.13 Statistical analysis

All data are presented as mean ± SEM, and statistical analyses were done using GraphPad Prism 6. Values that were not within the predetermined criterion of two SDs from the mean were considered statistical outliers and were excluded from the analysis. Unpaired *t* test with Welch's correction (two-tailed) was used for comparison of means of two groups. For comparisons between three or more groups, one-way ANOVA or two-way ANOVA (for two factors) with Fisher's LSD *post hoc* test was used to evaluate statistical significance, unless otherwise stated. Data with $p < 0.05$ was considered statistically significant. To determine the number of mice needed to reach statistical difference, power analysis was conducted, and sufficient number of mice was used in this study.

3 RESULTS

3.1 SFKs/Hck and Syk mediated Aβ oligomers (AβO)-stimulated activation of phagocytic activity in BV2 and primary microglial cells

To determine whether Hck and its downstream kinase, Syk, regulated the AβO-stimulated phagocytosis, we first stimulated BV2 cells with naturally secreted AβO from 7PA2 cells as collected in 7PA2-CM, along with well-established stimuli, mOZ and LPS, then quantified the phagocytic capacities of the cells. Like mOZ and LPS, AβO-stimulated BV2 cells elevated phagocytic efficiency (%) by three-fold (Figure 1a,b) and % phagocytic cells by nearly two-fold (Figure 1a,c) as compared to non-stimulated control or cells treated with basal CHO-CM. Pharmacological inhibition of SFKs/Hck by pan-Src inhibitor, PP2, or Syk by its specific inhibitor, BAY 61–3606, significantly attenuated AβO-induced phagocytic capacity of BV2 cells to the basal level, which were significantly lower ($p = 0.000011$–0.000192) than that of stimulus only treatment (Figure 1b,c). These data signify that the activation of BV2 cells phagocytosis by AβO stimulation was mediated in part by the SFKs/Hck and Syk pathways, and inactivation of either kinase significantly inhibited the phagocytic capacity of BV2 cells.

Hck and other SFKs are believed to regulate Syk activation through phosphorylation (Zhang, Billingsley, Kincaid, & Siraganian, 2000). Thus, we examined the phosphorylation status of Syk following co-treatment of pan-Src inhibitor with mOZ or 7PA2-CM in BV2 cells. We observed significant augmentation of Syk activation as indicated by the elevated levels of phosphorylated Syk at Tyr525/526 residues (pSyk) relative to total Syk by mOZ ($p = 0.0041$) and a trend towards increased pSyk by 7PA2-CM ($p = 0.0989$, Figure S1). Treatment with pan-Src inhibitor, PP2, significantly attenuated the levels of pSyk (mOZ: $p < 0.0001$; 7PA2-CM: $p = 0.0093$, Figure S1), confirming that Hck/SFKs mediated mOZ and AβO-stimulated BV2 phagocytic activities via Syk signaling pathway. We also assessed the protein levels of microglial pro-inflammatory marker, iNOS, and phagocytic marker, YM1, from the treated cells, but did not detect any modulation from the treatment condition (data not shown).

To further validate that AβO-stimulated microglial phagocytic activity was mediated via the Hck-Syk signaling pathway, we conducted *in vitro* phagocytosis assay in primary microglial cells after genetically knockdown Syk (Figure 2). Treating primary microglia derived from Syk/Cre mice with 4-OHT for two to four days, followed by culture medium at up to five days, resulted in a gradual reduction of Syk protein level down to ~21% relative to the untreated cells, implicating successful knockdown of majority of Syk in the primary microglial cells (Figure 2a). Substantial attenuation of primary microglial phagocytic activities were observed when the 4-OHT treatment condition was applied to the primary microglial cells prior to mOZ or 7PA2-CM stimulation (Figure 2b–d). Syk knockdown by 4-OHT treatment reduced the % phagocytic efficiency of AβO-stimulated primary microglia by 63% ($p = 0.0324$, Figure 2c) and % phagocytic cells by 44% ($p = 0.0083$, Figure 2d) relative to Syk intact cells. These data substantiate that Syk activity critically mediated AβO-stimulated primary microglial phagocytosis.

3.2 Genetic ablation of Hck significantly augmented Aβ plaque burden in J20 mouse model of AD

We next examined whether the genetic ablation of Hck exacerbated AD-like neuropathology at early plaque stage in the mouse model. Areas of Aβ plaques were measured in the hippocampus, cortex and amygdala, and taken relative to the entire area of the image as Aβ plaque burden. There were a five- ($p = 0.0048$) and four-fold ($p = 0.0594$) increase in 6E10-positive plaque burden in the hippocampus and cortex regions, respectively, of 6–8 months old J20/Hck-KO mice when compared to age-matched J20 mice (Figure 3a,b). Similar plaque burden accumulation was also observed in 4G8-positive plaques with nearly six- ($p = 0.0054$) and four-fold ($p = 0.0256$) increment found in the hippocampus and cortex regions of J20/Hck-KO mice, respectively (Figure 3a,c).

Given that the hippocampus is one of the earliest brain regions to be affected in AD (Braak, Braak, & Bohl, 1993) as well as in J20 mice (Mucke et al., 2000), we next quantified the level of $A\beta_{40}$ and $A\beta_{42}$ in detergent-soluble and -insoluble fractions of mouse hippocampal lysates using ELISA analysis. J20/Hck-KO mice did not alter soluble $A\beta_{40}$ and $A\beta_{42}$ levels significantly from J20 mice (Figure 3d). However, it induced a nearly three-fold increase in either $A\beta_{40}$ ($p = 0.003$) or $A\beta_{42}$ ($p = 0.001$) levels in the insoluble fraction as compared to J20 mice (Figure 3d). Insoluble $A\beta_{40}$ and $A\beta_{42}$ levels in J20/Hck-KO mice were also significantly higher than that of the WT and Hck-KO mice ($p < 0.0001$).

To examine whether the increased insoluble Aβ species were mediated by increase generation of Aβ in J20/Hck-KO mice, we quantified full length amyloid precursor protein (APP) and its C-terminal fragments (CTFs: C83 and C99) in the hippocampal lysates. While Hck ablation in J20 mice did not modulate the expression of full length APP from J20 mice, it significantly elevated the steady-state level of C83 fragment ($p = 0.0004$), but reduced that of C99 fragment ($p = 0.0395$) when compared to J20 mice (Supporting Information Figure S2a,b). In corroboration, we found lower levels of mature BACE1, a prerequisite enzyme for C99 fragment and Aβ formation (Cole & Vassar, 2007), in J20/Hck-KO mice relative to J20 mice ($p = 0.0354$, Supporting Information Figure S2c,d). Taken together, our results suggest that the exacerbated Aβ plaque deposition or insoluble Aβ accumulation in J20/Hck-KO mice was not likely to be mediated by increased APP production nor enhanced amyloidogenic pathway.

3.3 Hck deficiency modulated morphological phenotypes and activities in Aβ plaque-associated microglia

Given that clusters of activated microglia are commonly observed around Aβ plaques in postmortem human AD brains (Itagaki, McGeer, Akiyama, Zhu, & Selkoe, 1989; Mackenzie IR, Hao C, 1995; Wegiel & Wisniewski, 1990) and in AD mouse models, including J20 mice (Fu, Rusznák, Kwok, Kim, & Paxinos, 2014; Kim et al., 2013), we examined whether Hck deficiency perturbed such microglial phenotypes. We quantitatively measured the percent plaque area covered by $Iba1^+$ microglia and/or $CD45^+$ activated microglia at within 20 μm from the edge of the plaque, as described previously (Ulrich et al., 2014). Experimental bias was eliminated by comparing the distribution of plaque diameter between J20 and J20/Hck-KO mice and selecting the range of plaque size that was not significantly different for

analysis. We assessed microglia phenotypes around 6E10-labeled Aβ plaques and found a significant reduction in the plaque area covered by either Iba1$^+$ ($p = 0.0002$), Iba1$^+$ and CD45$^+$ ($p = 0.0206$), or Iba1$^+$ and CD45$^-$ ($p = 0.0253$) microglia in J20/Hck-KO mice (Figure 4a–d). Interestingly, there was no difference in the number of each type of microglia clustering the plaques (Figure 4e–g). Neither were differences observed in the total processes length per Iba1$^+$ microglia (Supporting Information Figure S3a) nor the number of Iba1$^+$ microglia branches (Supporting Information Figure S3b) around plaques between the genotypes. It appeared that the same number of microglia with similar morphologies was recruited to plaques, but covered the plaque area significantly lesser in J20/Hck-KO mice.

Having observed significant reduction in microglial phagocytosis after pharmacological inhibition of SFKs/Hck in BV2 cells, we examined whether genetic ablation of Hck in J20 mice recapitulated the same effect *in vivo*. Using confocal microscopy and Imaris volumetric and colocalization analysis, we quantified the volume of 6E10-positive plaques internalized in Iba1$^+$/CD68$^+$ microglial phagolysosomes as previously described (Marsh et al., 2016). Quantitative analysis of the Aβ internalization ratio revealed a significant 66% reduction in microglial phagocytic activity in J20/Hck-KO mice as compared to J20 mice ($p = 0.0159$, Figure 5).

Recent reports have shown that microglia play neuroprotective role by containing Thioflavin-S plaques with extended processes, thereby making them more compact and less diffuse (Condello, Yuan, Schain, & Grutzendler, 2015; Yuan et al., 2016). We examined these parameters using confocal microscopy and Imaris volumetric and automated analysis. While Hck deficiency did not modulate the Thioflavin-S plaque volume or the plaque intensity (Figure 6a and Supporting Information Figure S4a–b), there was a trend towards increasing number of Thioflavin-S plaques, specifically at all volumes ($p = 0.0866$) or at 500–1000 μm^3 ($p = 0.0714$; Supporting Information Figure S4c). In addition, the sphericity of Thioflavin-S plaques showed a tendency to be reduced ($p = 0.0788$) in J20/Hck-KO mice (Figure 6b), indicating that Hck deficiency partially resulted in more diffuse and less compact mature Aβ plaques. Analysis of Thioflavin-S plaque-associated microglia using Iba1-immunostaining showed that there was no change in the Thioflavin-S plaque volume covered by microglia per plaque volume per microglia between J20 and J20/Hck-KO mice (Figure 6c). Similarly, no difference was found in the number of microglia clustering around the plaques (Figure 6d) or in the volume of microglia clustering on Thioflavin-S plaques per plaque volume per microglia (Figure 6e). Further analysis of the microglial morphology showed no change in the total processes length of the microglia in each microglia (Figure 6f) but revealed a trend towards decreasing branching of the microglia ($p = 0.0756$) in J20/Hck-KO mice (Figure 6g). These data imply that the loss of Hck in J20 mice led to slightly more diffuse and less contained plaques surrounded by microglia with fewer branched processes.

Since our *in vivo* data indicated some functional alterations of microglia around plaques, we next explored for changes in cellular signaling and inflammatory responses in J20/Hck-KO mice. Microglia were co-stained with CD11b, iNOS, and pSyk antibodies. To correlate with the plaque-associated microglia analyzed in Figure 4, we examined only microglia that formed clusters and determined the expression levels of iNOS and/or pSyk in CD11b$^+$ microglial clusters and the number of cells expressing these markers (Figure 7).

Interestingly, we observed a four-fold increase in the iNOS expression at $p = 0.0147$ (Figure 7b), a three-fold increase in the pSyk level at $p = 0.016$ (Figure 7c), and a four-fold increase in the dual expression of iNOS and pSyk at $p = 0.0012$ (Figure 7d) in $CD11b^+$ microglia of J20/Hck-KO mice relative to age-matched J20 mice. While we did not find any difference in the number of $CD11b^+$ microglia forming clusters in the two mouse genotypes ($p = 0.3267$, Supporting Information Figure S5), a three-fold increase in the number of $CD11b^+$ microglia expressing iNOS ($p = 0.0142$, Figure 7e) or iNOS and pSyk ($p = 0.0206$, Figure 7g), and a two-fold increase in those expressing pSyk ($p = 0.0309$, Figure 7f) were observed in J20/Hck-KO mice. These findings implicate that the loss of Hck elevated Syk and microglial pro-inflammatory activation in microglial clusters around plaques.

3.4 Hck deletion moderately reduced steady-state and mRNA levels of Ym1 in J20 mice

We next examined whether Hck deficiency in J20 mice altered the protein levels of phagocytic markers, YM1 and Arg1, in the hippocampal tissues. Using Western blot analysis, we found a strong trend towards a reduction of YM1 in J20/Hck-KO mice when compared with J20 mice ($p = 0.0925$, Fisher's LSD *post hoc* test; Figure 8a,b). On the other hand, the protein level of Arg1 was much less different between the genotypes ($p = 0.1618$, one-way ANOVA, Figure 8a,b). The same trend was observed by real-time PCR analyses, showing that the Ym1 mRNA level was elevated in the hippocampi of J20 mice ($p = 0.0915$, one-way ANOVA with $p = 0.1444$ vs WT, $p = 0.0199$ vs Hck-KO, Fisher's LSD *post hoc* test; Figure 8c), but the elevation was reduced almost significantly in J20/Hck-KO mice ($p = 0.0654$ vs J20, Fisher's LSD *post hoc* test; Figure 8c). Interestingly, Ym1 mRNA was significantly reduced in the cortices of Hck-KO ($p = 0.0046$, Fisher's LSD *post hoc* test) and J20/Hck-KO mice ($p = 0.0252$, Fisher's LSD *post hoc* test) when compared to WT mice (Figure 8c). mRNA levels of Arg1 and Fizz1 were, however, unaltered in the hippocampi and cortices of all mice analyzed. Genetic ablation of Hck in J20 mice thus revealed trend of reduced hippocampal Ym1 protein and mRNA levels in J20/Hck-KO mice.

3.5 Changes in synaptic proteins and spine morphology in J20/Hck-KO mice

As one of the pathological features of AD is synaptic loss (DeKosky & Scheff, 1990; Terry et al., 1991), we investigated whether Hck deficiency in J20 mice would alter the spatial expression of pre-synaptic (synaptophysin) and post-synaptic (PSD95) proteins. PSD95 immunoreactivity was significantly reduced in the hippocampal DG ($p = 0.0025$ vs J20 mice, Fisher's LSD *post hoc* test) and CA3 ($p = 0.0022$ vs J20 mice, Fisher's LSD *post hoc* test) regions, but revealed a trend towards reduction in the CA1 region of J20/Hck-KO mice (Figure 9a,b). Similarly, synaptophysin immunoreactivity in J20/Hck-KO mice showed trend of reduction in the DG ($p = 0.09$, one-way ANOVA), CA1 ($p = 0.2954$, one-way ANOVA) and CA3 regions ($p = 0.0134$, one-way ANOVA; $p = 0.0548$ vs J20 mice, Fisher's LSD *post hoc* test, Supporting Information Figure S6.) Conversely, we did not find significant difference in the PSD95 or synaptophysin immunoreactivity between WT, Hck-KO and J20 mice.

Next, we proceed to examine the dendritic spine morphology on the pyramidal neurons in the CA1 region, which is important for learning and memory (Kerchner & Nicoll, 2008), and commonly found atrophy in AD patients (Kerchner et al., 2012). Dendritic spines were

classified according to their types, namely filopodia, stubby and thin as immature spine or mushroom and branched as mature spine in the hippocampus (Penazzi et al., 2016; van der Zee, 2015). Quantification of spine types relative to the length of the dendrites revealed a significant reduction of mushroom spine in J20/Hck-KO mice when compared with either WT (31%, $p = 0.0440$) or Hck-KO (37%, $p = 0.0110$, Figure 9c,d). However, no significant difference in the number of any types of spines analyzed was detected between J20 and J20/Hck-KO mice. When we analyzed immature (filopodia, stubby and thin) and mature (mushroom and branched) spines relative to total number of spines, J20/Hck-KO mice showed significantly more immature spines and less mature spines than WT (immature: 32% increase, $p = 0.0419$; mature: 29% decrease, $p = 0.0419$) or Hck-KO (immature: 47% increase, $p = 0.0106$; mature: 35% decrease, $p = 0.0106$) mice (Figure 9e). We also found an increased trend of immature spines and reduced trend of mature spines in J20/Hck-KO mice relative to J20 mice (Figure 9e). Taken together, the loss of mature spines in J20/Hck-KO was clearly evident when compared to WT or Hck-KO mice, but it was fairly marginal when compared to J20 mice.

3.6 Hck deficiency did not alter cognition in early plaque stage of J20 mice

To determine whether Hck deficiency accelerated cognitive decline in J20 mice, we tested mice for non-spatial recognition memory (NOR) and spatial recognition memory (OIP and MWM). No significant differences were detected in WT, Hck-KO, J20, and J20/Hck-KO mice in NOR or OIP tests (Figure 10a,b). In MWM, while J20 mice exhibited an impaired acquisition memory during the training, that of J20/Hck-KO mice were not significantly impaired when compared to WT or Hck-KO (Figure 10c). In the probe trials, no significant difference was observed between the mouse genotypes in terms of escape latency ($p = 0.4426$ for 72 h, $p = 0.0796$ for 1 wk; Figure 10d), number of platform crosses ($p = 0.0539$ for 72 h, $p = 0.0642$ for 1 wk; Figure 10e), and time spend in the target ($p = 0.7383$ for 72 h, $p = 0.7069$ for 1 wk; Figure 10f) or opposite quadrant ($p = 0.8768$ for 72 h, $p = 0.4433$ for 1 wk; Supporting Information Figure S7a) by one-way ANOVA analysis. There was also no difference observed in the total distance that mice swam and swim speed of the mice between the genotypes (Supporting Information Figure S7b,c).

4 DISCUSSION

Emerging evidence have shown that microglia exhibit impaired phagocytic activity that contribute to Aβ deposition and subsequent AD pathology (Malm et al., 2015; Mosher & Wyss-Coray, 2014). Thus, understanding the molecular mechanisms that derail proper microglial phagocytic activity in AD is crucial in delineating the pathogenesis of AD. Hck is a phagocyte-specific tyrosine kinase among the SFKs (Guiet et al., 2008; Lowell, Soriano, & Varmus, 1994) and possesses significant regulatory strength and altered expression in the microglia of sporadic AD patients (Zhang et al., 2013). Hck signaling pathways have been implicated in diseases involving phagocytes, such as inflammatory diseases, human immunodeficiency virus-1 (HIV-1) infections and leukemia (Guiet et al., 2008). However, there is no report on the molecular assessment of Hck signaling in AD pathogenesis to date. On the contrary, Syk has been shown to be activated by tyrosine phosphorylation by the SFKs upon stimulated with Aβ (Combs, Johnson, Cannady, Lehman, & Landreth, 1999;

McDonald, Brunden, & Landreth, 1997; Sondag, Dhawan, & Combs, 2009) and mediated fibrillar Aβ-stimulated microglial phagocytosis (Koenigsknecht & Landreth, 2004). Nonetheless, the involvement of Syk in mediating AβO-stimulated microglial phagocytosis has not been shown.

Our *in vitro* BV2 cells phagocytosis assay showed that AβO at physiological levels as found in human AD brains (Calabrese et al., 2007) stimulated phagocytosis via Hck/SFKs and Syk activation, implicating the involvement of these kinases in the neuroprotective role of microglia in AD. Our *in vitro* findings are in part supported by existing literature showing that PP2 as well as MNS, a Src/Syk inhibitor, significantly attenuated BV2 cells phagocytic activities (Koenigsknecht & Landreth, 2004; Marsh et al., 2016), substantiating the involvement of SFKs and Syk in mediating AβO-stimulated BV2 cells phagocytosis. Notwithstanding that, we have also demonstrated that Syk mediated AβO-stimulated phagocytosis in primary microglial cells, signifying the neuroprotective role of Hck/SFKs and its downstream kinase, Syk, in mediating microglial clearance of AβO.

Corroborating with our *in vitro* study, we report novel findings that deleting Hck in J20 mice significantly augmented Aβ plaque deposition in the hippocampus and cortex, with no observable change in the full length APP. On the other hand, we detected a significant reduction in C99 fragment in J20/Hck-KO mice that correlated with the drastic decrease in mature BACE1 level. BACE1 is an initial and rate-limiting enzyme for Aβ formation (Cole & Vassar, 2007) by first producing C99 fragment. It is interesting to observe attenuation of both C99 fragment and mature BACE1 levels when Hck was genetically ablated from either WT or J20 mice. While we cannot fully explain if Hck deletion has any significant consequence on the mature BACE1 activity or subsequent alteration in the APP processing in this study, our observations may provide a clue that biological functions of Hck in neurons may be detrimental, and inhibiting Hck in neurons could be neuroprotective by suppressing BACE1 maturation, as opposed to its potentially beneficial functions in microglia shown in this study. Nonetheless, such diverse cell type-specific biological effects of Hck should be examined in more detail. In contrast to the level of C99 fragment, an elevation of C83 fragment was observed in J20/Hck-KO mice. This further substantiates the lack of enhanced APP amyloidogenic metabolism as a reciprocal relationship between non-amyloidogenic and amyloidogenic APP processing has been reported in previous studies (Skovronsky, Moore, Milla, Doms, & Lee, 2000; Vassar et al., 1999).

Our *in vivo* results also suggest that Hck deficiency promotes microglia towards more pro-inflammatory state, which has been observed in longitudinal studies of microglial activation phenotypes in APP/PS1 AD mouse model (Jimenez et al., 2008) and in human AD patients (Fan, Brooks, Okello, & Edison, 2017). In the mouse model study, Jimenez et al. observed an apparent reduction of Ym1 mRNA coupled with significant induction of iNos and Tnfα mRNA levels when comparing the hippocampi of 6 and 18 months old APP/PS1 mice (Jimenez et al., 2008). Interestingly, the authors did not detect any modulation in the mRNA level of Arg1 as in our study. Likewise in the human study, Fan et al. suggested that once microglia fail to clear Aβ in the early stage of AD, plaques will be accumulated, leading to a decrease in anti-inflammatory but increase in pro-inflammatory microglial activation (Fan, Brooks, Okello, & Edison, 2017). Our data are in accordance to these notions in that

deleting Hck, a primary regulator of phagocytosis in the SFKs, in J20 mice partially accelerated the impairment of anti-inflammatory state and Aβ clearance capacity of microglia by phagocytosis, while promoted microglial pro-inflammatory activation and buildup of Aβ plaque burden.

Besides reduced microglial Aβ phagocytosis and plaque clearance, our data showed evidence of dysregulation in microglia envelopment around the more mature Thioflavin-S-positive plaques and less mature 6E10-immunoreactive plaques in J20/Hck-KO mice. Condello et al. demonstrated in their 2015 study that microglia play a neuroprotective role by forming a barrier around toxic protofibrillar plaques to prevent neuritic dystrophy (Condello et al., 2015), which is supported by a recent study (Zhao, Hu, Tsai, Li, & Gan, 2017). Condello's study was followed up by Yuan and colleagues (Yuan et al., 2016) who reported that removing microglial immunoreceptor - triggering receptor expressed on myeloid cells 2 (TREM2), or its adaptor protein - DNAX-binding protein of 12 kDa (DAP12), which acts upstream of SFKs and Syk (Colonna & Wang, 2016), reduced microglia envelopment and plaque compaction in AD mice that contributed to severe axonal dystrophy. Similar observations of reduced microglia coverage around Aβ plaques owing to TREM2 deficiency were also made by other groups (Jay et al., 2017; Wang et al., 2016). Consistent with these findings, we observed trend of less spherical ie. more diffuse Thioflavin-S plaques clustered by fewer branched microglia when removing Hck in J20 mice. This implicates that Hck deficiency in J20 mice partially reduced microglial containment capability that resulted in more diffuse or less compact mature Aβ plaques. Likewise for 6E10-immunoreactive Aβ plaques, we detected a significant reduction in the plaque coverage by Hck-deficient microglia with concomitant increase in the plaque deposition. There is, however, some distinctions here, in that morphologically similar and same number of microglia were recruited to the less mature 6E10-positive plaques, but Hck removal seemingly resulted in smaller microglial clusters covering the plaques than that observed in Hck-sufficient J20 mice. This could, in part, affect the phagocytic efficiency of the Hck-deficient microglia, since they were less accessible to the plaques.

We noted that there was no change in the dendritic spine morphology of J20 mice when compared with the non-AD mice in the CA1 region at 6–8 months old. This corroborates with the findings of Pujadas and colleagues (Pujadas et al., 2014), while other studies demonstrated that dendritic spines loss in the CA1 region were usually observed in J20 mice of 9 months and older (Moolman, Vitolo, Vonsattel, & Shelanski, 2004; Pozueta et al., 2013). On the other hand, Hck deletion in J20 mice significantly increased the % immature and decreased the % mature spines from that of the non-AD mice, but did not mediate dramatic changes from that of J20 mice. The lack of drastic modulation in the CA1 dendritic spine morphology by J20/Hck-KO mice was also reflected in the lack of significant changes in the spatial expression of PSD95 in the same region. On the contrary, Hck deletion in J20 mice resulted in significant reductions of PSD95 immunoreactivity in the DG and CA3 regions when compared to J20 mice. The modulation, however, did not lead to cognitive deficits as observed in our behavioral tests. Neither were any cognitive impairments observed in our 5–6 months old J20 mice. It is apparent that the consequence of Hck elimination in the pathologically young J20 mice elicited an early neuropathological development, with increased plaque disposition and microglial dysfunction and

inflammation, but the effects were not sufficient to impair cognitive function. This is plausible since deficiency of TREM2 - another microglial activation modulator - revealed exacerbated AD-like pathology only at the later stage of the disease (Jay et al., 2017).

There are evidence that high levels of pSyk were expressed in hyperactive microglia of AD mouse models and human AD brains (Satoh et al., 2012; Schweig et al., 2017), which contributed to the secretion of pro-inflammatory cytokines upon stimulated by Aβ species (Combs, Karlo, Kao, & Landreth, 2001; Sondag, Dhawan, & Combs, 2009). While we did not observe such microglial phenotypes in our pathologically young J20 mice yet, we detected elevated levels of pSyk and iNOS with Hck ablation. This signifies that Hck plays a more pivotal role than other SFKs in regulating microglial activities and neuroinflammation. It is noteworthy that high levels of iNOS in activated microglia has been reported to produce nitric oxide (NO) that impaired phagocytic activities (Kopec & Carroll, 2000). In accordance to this, we observed augmented iNOS expression and dramatic attenuation in Aβ internalization owing to impaired phagocytosis in our Hck-deficient microglial cells. Taken together, these prompt towards an existence of a cause-effect relationship whereby Aβ species initially stimulated microglia to phagocytose Aβ via Hck/Syk signaling pathways, but upon chronic activation of microglia, the Syk signaling switched from activating phagocytosis to triggering pro-inflammatory cytokines, such as iNOS, that released NO and impaired further clearance of Aβ by phagocytosis.

The current study demonstrates that Hck plays a multifactorial role in regulating microglial Aβ phagocytosis and plaque envelopment that facilitate Aβ clearance and containment. Loss of Hck in J20 mice resulted in exacerbated Aβ deposition and significant reduction of PSD95 protein level in hippocampal DG and CA3 regions, despite the presence of other members of the SFKs that could compensate for the function of Hck. Furthermore, significant activation of the pro-inflammatory state microglia was observed, implicating that loss of Hck alone is sufficient to accelerate microglia class switch from neuroprotective phenotype to neuroinflammation type, which is usually observed in aging AD mouse model and patients. We conclude that Hck is a likely therapeutic target for early intervention of AD progression.

Supplementary Material

Refer to Web version on PubMed Central for supplementary material.

ACKNOWLEDGEMENTS

We thank the following people for their kind contribution and assistance: Dr. Edward Koo (University of California, San Diego) for the 7PA2 and CHO cells; Dr. Gary Landreth (Case Western Reserve University) for the BV2 cells; Dr. Tatsuhide Tanaka (Asahikawa Medical University) for the protocol for isolating primary microglia; Dr. Clifford Lowell (University of California, San Francisco) for the Hck-KO mice; Dr. Vitaly Vasilevko and Dr. David H. Cribbs (University of California, Irvine) for the $A\beta_{40}$ and $A\beta_{42}$ antibodies for ELISA; Dr. David Baglietto-Vargas (University of California, Irvine) for his technical support on Stereology and Confocal Microscopy, and Dr. Samuel E. Marsh (University of California, Irvine) for his guidance on Imaris analysis.

FUNDING

This study was supported by the NIH/NIEHS R01 ES024331, Alzheimer's Association (NIRG-12–242598 and AARF-16–440554), and OD010420 (FML).

ABBREVIATIONS

AD	Alzheimer's disease
Aβ	Amyloid-β
Hck	Hematopoietic cell kinase
Syk	Spleen tyrosine kinase
SFKs	Src family tyrosine kinases
J20/Hck-KO mice	Hck-deficient J20 mice
Hck-KO	Hck-knocked out
WT	wild-type
CHO cells	Chinese hamster ovary cells
7PA2 cells	transfected CHO cells that express V717F AD mutation in amyloid-β precursor protein 751
CM	Conditioned medium
DMEM	Dulbecco's Modified Eagle's medium
FBS	fetal bovine serum
SFM	Serum free medium
4-OHT	4-hydroxytamoxifen
mOZ	mouse complement-opsonized zymosan
LPS	lipopolysaccharide
PBS	phosphate buffered saline
PFA	paraformaldehyde
ELISA	enzyme-linked immunosorbent assay
PCR	polymerase chain reaction
NOR	Novel Object Recognition
RI	Recognition index
OIP	Object In Place
MWM	Morris Water Maze
AβO	Amyloid-β oligomers
APP	Amyloid precursor protein

CTFs	C-terminal fragments
BACE1	Beta-site amyloid precursor protein cleaving enzyme 1
iNOS	inducible nitric oxide synthase
pSyk	phosphorylated spleen tyrosine kinase
SR	stratum radiatum
TREM2	Triggering receptor expressed on myeloid cells 2
DAP12	DNAX-binding protein of 12 kDa
NO	nitric oxide

REFERENCES

Beauquis J, Vinuesa A, Pomilio C, Pavía P, Galván V, & Saravia F (2014). Neuronal and glial alterations, increased anxiety, and cognitive impairment before hippocampal amyloid deposition in PDAPP mice, model of Alzheimer's disease. Hippocampus, 24(3), 257–269. 10.1002/hipo.22219 [PubMed: 24132937]

Braak H, Braak E, & Bohl J (1993). Staging of Alzheimer-related cortical destruction. European Neurology, 33(6), 403–408. [PubMed: 8307060]

Calabrese B, Shaked GM, Tabarean IV, Braga J, Koo EH, & Halpain S (2007). Rapid, Concurrent Alterations in Pre- and Postsynaptic Structure Induced by Soluble Natural Amyloid-β Protein. Molecular and Cellular Neuroscience, 35(2), 183–193. [PubMed: 17368908]

Choucair N, Laporte V, Levy R, Arnold AS, Gies JP, Poindron P, & Lombard Y (2006). Phagocytic functions of microglial cells in the central nervous system and their importance in two neurodegenerative diseases: Multiple sclerosis and Alzheimer's disease. Central European Journal of Biology, 1(4), 463–493. 10.2478/s11535-006-0038-y

Cole SL, & Vassar R (2007). The Alzheimer's disease Beta-secretase enzyme, BACE1. Molecular Neurodegeneration, 2(1), 22 10.1186/1750-1326-2-22 [PubMed: 18005427]

Colonna M, & Wang Y (2016). TREM2 variants: new keys to decipher Alzheimer disease pathogenesis. Nature Reviews Neuroscience, 17(4), 201–207. 10.1038/nrn.2016.7 [PubMed: 26911435]

Combs CK, Johnson DE, Cannady SB, Lehman TM, & Landreth GE (1999). Identification of microglial signal transduction pathways mediating a neurotoxic response to amyloidogenic fragments of beta-amyloid and prion proteins. Journal of Neuroscience, 19(3), 928–39. [PubMed: 9920656]

Combs CK, Karlo JC, Kao SC, & Landreth GE (2001). beta-Amyloid stimulation of microglia and monocytes results in TNFalpha-dependent expression of inducible nitric oxide synthase and neuronal apoptosis. Journal of Neuroscience, 21(4), 1179–88. [PubMed: 11160388]

Condello C, Yuan P, Schain A, & Grutzendler J (2015). Microglia constitute a barrier that prevents neurotoxic protofibrillar Aβ42 hotspots around plaques. Nature Communications, 6, 6176 10.1038/ncomms7176

Cunningham C (2013). Microglia and neurodegeneration: The role of systemic inflammation. Glia, 61(1), 71–90. 10.1002/glia.22350 [PubMed: 22674585]

DeKosky ST, & Scheff SW (1990). Synapse loss in frontal cortex biopsies in Alzheimer's disease: correlation with cognitive severity. Annals of Neurology, 27(5), 457–464. 10.1002/ana.410270502 [PubMed: 2360787]

Dhawan G, & Combs CK (2012). Inhibition of Src kinase activity attenuates amyloid associated microgliosis in a murine model of Alzheimer's disease. Journal of Neuroinflammation, 9, 117 10.1186/1742-2094-9-117 [PubMed: 22673542]

Dhawan G, Floden AM, & Combs CK (2012). Amyloid-β oligomers stimulate microglia through a tyrosine kinase dependent mechanism. Neurobiology of Aging, 33(10), 2247–2261. 10.1016/j.neurobiolaging.2011.10.027.Amyloid- [PubMed: 22133278]

Dunn HC, Ager RR, Baglietto-Vargas D, Cheng D, Kitazawa M, Cribbs DH, & Medeiros R (2015). Restoration of lipoxin A4 signaling reduces Alzheimer's disease-like pathology in the 3xTg-AD mouse model. Journal of Alzheimer's Disease, 43(3), 893–903. 10.3233/JAD-141335

Eikelenboom P, Bate C, Van Gool WA, Hoozemans JJM, Rozemuller JM, Veerhuis R, & Williams A (2002). Neuroinflammation in Alzheimer's disease and prion disease. Glia, 40(2), 232–239. 10.1002/glia.10146 [PubMed: 12379910]

Fan Z, Brooks DJ, Okello A, & Edison P (2017). An early and late peak in microglial activation in Alzheimer's disease trajectory. Brain, 40(3), 792–803. 10.1093/brain/aww349

Fu Y, Rusznák Z, Kwok J, Kim WS, & Paxinos G (2014). Age-Dependent Alterations of the Hippocampal Cell Composition and Proliferative Potential in the hAβPPSwInd-J20 Mouse. Journal of Alzheimer's Disease, 41(4), 1177–92. 10.3233/JAD-132717

Guiet R, Poincloux R, Castandet J, Marois L, Labrousse A, Le Cabec V, & Maridonneau-Parini I (2008). Hematopoietic cell kinase (Hck) isoforms and phagocyte duties - From signaling and actin reorganization to migration and phagocytosis. European Journal of Cell Biology, 87(8–9), 527–542. 10.1016/j.ejcb.2008.03.008 [PubMed: 18538446]

Itagaki S, McGeer PL, Akiyama H, Zhu S, & Selkoe D (1989). Relationship of microglia and astrocytes to amyloid deposits of Alzheimer disease. Journal of Neuroimmunology, 24(3), 173–182. [PubMed: 2808689]

Jay TR, Hirsch XAM, Broihier XML, Miller XCM, Neilson XLE, Ransohoff XRM, … Landreth GE (2017). Disease Progression-Dependent Effects of TREM2 Deficiency in a Mouse Model of Alzheimer's Disease. Journal of Neuroscience, 37(3), 637–647. 10.1523/JNEUROSCI.2110-16.2017 [PubMed: 28100745]

Jimenez S, Baglietto-Vargas D, Caballero C, Moreno-Gonzalez I, Torres M, Sanchez-Varo R, … Vitorica J (2008). Inflammatory response in the hippocampus of PS1M146L/APP751SL mouse model of Alzheimer's disease: age-dependent switch in the microglial phenotype from alternative to classic. Journal of Neuroscience, 28(45), 11650–11661. 10.1523/JNEUROSCI.3024-08.2008 [PubMed: 18987201]

Kerchner GA, Deutsch GK, Zeineh M, Dougherty RF, Saranathan M, & Rutt BK (2012). Hippocampal CA1 apical neuropil atrophy and memory performance in Alzheimer's disease. NeuroImage, 63(1), 194–202. 10.1016/j.neuroimage.2012.06.048 [PubMed: 22766164]

Kerchner GA, & Nicoll RA (2008). Silent synapses and the emergence of a postsynaptic mechanism for LTP. Nature Reviews Neuroscience, 9(11), 813–825. 10.1038/nrn2501 [PubMed: 18854855]

Kim WS, Li H, Ruberu K, Chan S, Elliott D. a, Low JK, … Garner B (2013). Deletion of Abca7 increases cerebral amyloid-β accumulation in the J20 mouse model of Alzheimer's disease. Journal of Neuroscience, 33(10), 4387–94. 10.1523/JNEUROSCI.4165-12.2013 [PubMed: 23467355]

Kitazawa M, Cheng D, Tsukamoto MR, Koike M. a, Wes PD, Vasilevko V, … LaFerla FM (2011). Blocking IL-1 signaling rescues cognition, attenuates tau pathology, and restores neuronal β-catenin pathway function in an Alzheimer's disease model. Journal of Immunology, 187(12), 6539–49. 10.4049/jimmunol.1100620

Koenigsknecht-Talboo J, & Landreth GE (2005). Microglial phagocytosis induced by fibrillar beta-amyloid and IgGs are differentially regulated by proinflammatory cytokines. Journal of Neuroscience, 25(36), 8240–9. 10.1523/JNEUROSCI.1808-05.2005 [PubMed: 16148231]

Koenigsknecht J, & Landreth G (2004). Microglial phagocytosis of fibrillar beta-amyloid through a beta1 integrin-dependent mechanism. Journal of Neuroscience, 24(44), 9838–46. 10.1523/JNEUROSCI.2557-04.2004 [PubMed: 15525768]

Kopec K, & Carroll R (1998). Alzheimer's beta-amyloid peptide 1–42 induces a phagocytic response in murine microglia. Journal of Neurochemistry, 71(5), 2123–2131. 10.1046/j.1471-4159.1998.71052123.x [PubMed: 9798938]

Kopec K, & Carroll R (2000). Phagocytosis is regulated by nitric oxide in murine microglia. Nitric Oxide - Biology and Chemistry, 4(2), 103–111. 10.1006/niox.2000.0280 [PubMed: 10835290]

Lim SL, Rodriguez-Ortiz CJ, & Kitazawa M (2015). Infection, systemic inflammation, and Alzheimer's disease. Microbes and Infection, 17(8), 549–556. 10.1016/j.micinf.2015.04.004 [PubMed: 25912134]

Linnartz B, & Neumann H (2013). Microglial activatory (immunoreceptor tyrosine-based activation motif)- and inhibitory (immunoreceptor tyrosine-based inhibition motif)-signaling receptors for recognition of the neuronal glycocalyx. Glia, 61(1), 37–46. 10.1002/glia.22359 [PubMed: 22615186]

Livak KJ, & Schmittgen TD (2001). Analysis of relative gene expression data using real-time quantitative PCR and the 2-ΔΔCt Method. Methods, 25, 402–408. 10.1006/meth.2001.1262 [PubMed: 11846609]

Lowell CA (2011). Src-family and Syk kinases in activating and inhibitory pathways in innate immune cells: signaling cross talk. Cold Spring Harbor Perspectives in Biology, 3(3), a002352 10.1101/cshperspect.a002352 [PubMed: 21068150]

Lowell CA, Soriano P, & Varmus HE (1994). Functional overlap in the src gene family: Inactivation of hck and fgr impairs natural immunity. Genes & Development, 8(4), 387–398. 10.1101/gad.8.4.387 [PubMed: 8125254]

Mackenzie IR, Hao C, M. D (1995). Role of microglia in senile plaque formation. Neurobiology of Aging, 16(5), 797–804. [PubMed: 8532113]

Malm TM, Jay TR, & Landreth GE (2015). The Evolving Biology of Microglia in Alzheimer's Disease. Neurotherapeutics, 12(1), 81–93. 10.1007/s13311-014-0316-8 [PubMed: 25404051]

Marsh SE, Abud EM, Lakatos A, Karimzadeh A, Yeung ST, Davtyan H, … Blurton-Jones M (2016). The adaptive immune system restrains Alzheimer's disease pathogenesis by modulating microglial function. Proceedings of the National Academy of Sciences, 113(9), E1316–25. 10.1073/pnas.1525466113

Mawuenyega KG, Sigurdson W, Ovod V, Munsell L, Kasten T, Morris JC, … Bateman RJ (2010). Decreased Clearance of CNS beta-amyloid in Alzheimer's Disease. Science, 330(6012), 1774 10.1126/science.1197623.Decreased [PubMed: 21148344]

McDonald DR, Brunden KR, & Landreth GE (1997). Amyloid fibrils activate tyrosine kinase-dependent signaling and superoxide production in microglia. Journal of Neuroscience, 17(7), 2284–94. [PubMed: 9065490]

Medeiros R, Kitazawa M, Caccamo A, Baglietto-Vargas D, Estrada-Hernandez T, Cribbs DH, … LaFerla FM (2011). Loss of muscarinic M1 receptor exacerbates Alzheimer's disease-like pathology and cognitive decline. American Journal of Pathology, 179(2), 980–991. 10.1016/j.ajpath.2011.04.041 [PubMed: 21704011]

Medeiros R, Kitazawa M, Passos GF, Baglietto-Vargas D, Cheng D, Cribbs DH, & LaFerla FM (2013). Aspirin-triggered lipoxin A4 stimulates alternative activation of microglia and reduces Alzheimer disease-like pathology in mice. American Journal of Pathology, 182, 1780–1789. 10.1016/j.ajpath.2013.01.051 [PubMed: 23506847]

Moolman DL, Vitolo OV, Vonsattel JPG, & Shelanski ML (2004). Dendrite and dendritic spine alterations in Alzheimer models. Journal of Neurocytology, 33(3), 377–387. 10.1023/B:NEUR.0000044197.83514.64 [PubMed: 15475691]

Mosher KI, & Wyss-Coray T (2014). Microglial dysfunction in brain aging and Alzheimer's disease. Biochemical Pharmacology, 88(4), 594–604. 10.1016/j.bcp.2014.01.008 [PubMed: 24445162]

Mucke L, Masliah E, Yu GQ, Mallory M, Rockenstein EM, Tatsuno G, … McConlogue L (2000). High-level neuronal expression of abeta 1–42 in wild-type human amyloid protein precursor transgenic mice: synaptotoxicity without plaque formation. Journal of Neuroscience, 20(11), 4050–8. [PubMed: 10818140]

Ozaki N, Suzuki S, Ishida M, Harada Y, Tanaka K, Sato Y, … Yoshida H (2012). Syk-dependent signaling pathways in neutrophils and macrophages are indispensable in the pathogenesis of anti-collagen antibody-induced arthritis. International Immunology, 24(9), 539–50. 10.1093/intimm/dxs078 [PubMed: 22914861]

Pan X, Zhu Y, Lin N, Zhang J, Ye Q, Huang H, & Chen X (2011). Microglial phagocytosis induced by fibrillar β-amyloid is attenuated by oligomeric β -amyloid: implications for Alzheimer's disease. Molecular Neurodegeneration, 45(6), 1–17.

Penazzi L, Tackenberg C, Ghori A, Golovyashkina N, Niewidok B, Selle K, … Brandt R (2016). Aβ-mediated spine changes in the hippocampus are microtubule-dependent and can be reversed by a subnanomolar concentration of the microtubule-stabilizing agent epothilone D. Neuropharmacology, 105, 84–95. 10.1016/j.neuropharm.2016.01.002 [PubMed: 26772969]

Pozueta J, Lefort R, Ribe E, Troy C, Arancio O, & Shelanski M (2013). Caspase-2 is required for dendritic spine and behavioural alterations in J20 APP transgenic mice. Nature Communications, 4, 1939 10.1001/jamasurg.2014.1086.Feasibility

Pujadas L, Rossi D, Andrés R, Teixeira CM, Serra-Vidal B, Parcerisas A, … Soriano E (2014). Reelin delays amyloid-beta fibril formation and rescues cognitive deficits in a model of Alzheimer's disease. Nature Communications, 5, 3443 10.1038/ncomms4443

Querfurth HW, & LaFerla FM (2010). Alzheimer's disease. The New England Journal of Medicine, 362(4), 329–344. 10.1056/NEJMra0909142 [PubMed: 20107219]

Rodriguez-Ortiz CJ, Hoshino H, Cheng D, Liu-Yescevitz L, Blurton-Jones M, Wolozin B, … Kitazawa M (2013). Neuronal-specific overexpression of a mutant valosin-containing protein associated with IBMPFD promotes aberrant ubiquitin and TDP-43 accumulation and cognitive dysfunction in transgenic mice. American Journal of Pathology, 183(2), 504–15. 10.1016/j.ajpath.2013.04.014 [PubMed: 23747512]

Satoh J-I, Tabunoki H, Ishida T, Yagishita S, Jinnai K, Futamura N, … Arima K (2012). Phosphorylated Syk expression is enhanced in Nasu-Hakola disease brains. Neuropathology, 32(2), 149–57. 10.1111/j.1440-1789.2011.01256.x [PubMed: 21981270]

Schweig JE, Yao H, Beaulieu-Abdelahad D, Ait-Ghezala G, Mouzon B, Crawford F, … Paris D (2017). Alzheimer's disease pathological lesions activate the spleen tyrosine kinase. Acta Neuropathologica Communications, 5(1), 69 10.1186/s40478-017-0472-2 [PubMed: 28877763]

Skovronsky DM, Moore DB, Milla ME, Doms RW, & Lee VM (2000). Protein kinase C-dependent alpha-secretase competes with beta-secretase for cleavage of amyloid-beta precursor protein in the trans-golgi network. The Journal of Biological Chemistry, 275(4), 2568–2575. 10.1074/jbc.275.4.2568 [PubMed: 10644715]

Sondag CM, Dhawan G, & Combs CK (2009). Beta amyloid oligomers and fibrils stimulate differential activation of primary microglia. Journal of Neuroinflammation, 6(1), 1 10.1186/1742-2094-6-1 [PubMed: 19123954]

Song S, Zhou F, & Chen WR (2012). Low-level laser therapy regulates microglial function through Src-mediated signaling pathways: implications for neurodegenerative diseases. Journal of Neuroinflammation, 9(219), 1–17. 10.1186/1742-2094-9-219 [PubMed: 22212381]

Tanaka T, Murakami K, Bando Y, & Yoshida S (2015). Interferon regulatory factor 7 participates in the M1-like microglial polarization switch. Glia, 63(4), 595–610. 10.1002/glia.22770 [PubMed: 25422089]

Tarasoff-Conway JM, Carare RO, Osorio RS, Glodzik L, Butler T, Fieremans E, … de Leon MJ (2015). Clearance systems in the brain-implications for Alzheimer disease. Nature Reviews Neurology, 11(8), 457–70. 10.1038/nrneurol.2015.119 [PubMed: 26195256]

Terry RD, Masliah E, Salmon DP, Butters N, DeTeresa R, Hill R, … Katzman R (1991). Physical basis of cognitive alterations in Alzheimer's disease: synapse loss is the major correlate of cognitive impairment. Annals of Neurology, 30(4), 572–580. 10.1002/ana.410300410 [PubMed: 1789684]

Ulrich JD, Finn MB, Wang Y, Shen A, Mahan TE, Jiang H, … Holtzman DM (2014). Altered microglial response to Abeta plaques in APPPS1–21 mice heterozygous for TREM2. Molecular Neurodegeneration, 9(1), 20 10.1186/1750-1326-9-20 [PubMed: 24893973]

van der Zee EA (2015). Synapses, spines and kinases in mammalian learning and memory, and the impact of aging. Neuroscience and Biobehavioral Reviews, 50, 77–85. 10.1016/j.neubiorev.2014.06.012 [PubMed: 24998408]

Vassar R, Bennett BD, Babu-Khan S, Kahn S, Mendiaz EA, Denis P, … Citron M (1999). β-Secretase cleavage of Alzheimer's amyloid precursor protein by the transmembrane aspartic protease BACE. Science, 286(5440), 735–741. 10.1126/science.286.5440.735 [PubMed: 10531052]

Walsh DM, Klyubin I, Fadeeva JV, Cullen WK, Anwyl R, Wolfe MS, … Selkoe DJ (2002). Naturally secreted oligomers of amyloid beta protein potently inhibit hippocampal long-term potentiation in vivo. Nature, 416(6880), 535–9. 10.1038/416535a [PubMed: 11932745]

Wang Y, Ulland TK, Ulrich JD, Song W, Tzaferis JA, Hole JT, … Colonna M (2016). TREM2-mediated early microglial response limits diffusion and toxicity of amyloid plaques. Journal of Experimental Medicine, 213(5), 667–75. 10.1084/jem.20151948 [PubMed: 27091843]

Wegiel J, & Wisniewski H (1990). The complex of microglial cells and amyloid star in three-dimensional reconstruction. Annals of Neurology, 81(2), 116–24.

Wes PD, Sayed FA, Bard F, & Gan L (2016). Targeting microglia for the treatment of Alzheimer's Disease. Glia, 64(10), 1710–1732. 10.1002/glia.22988 [PubMed: 27100611]

Wildsmith KR, Holley M, Savage JC, Skerrett R, & Landreth GE (2013). Evidence for impaired amyloid β clearance in Alzheimer's disease. Alzheimer's Research & Therapy, 5(4), 33 10.1186/alzrt187

Wood JG, & Zinsmeister P (1991). Tyrosine phosphorylation systems in Alzheimer's disease pathology. Neuroscience Letters, 121(1–2), 12–16. [PubMed: 1708471]

Yuan P, Condello C, Keene CD, Wang Y, Bird TD, Paul SM, … Grutzendler J (2016). TREM2 Haplodeficiency in Mice and Humans Impairs the Microglia Barrier Function Leading to Decreased Amyloid Compaction and Severe Axonal Dystrophy. Neuron, 90(4), 724–739. 10.1016/j.neuron.2016.05.003 [PubMed: 27196974]

Zhang B, Gaiteri C, Bodea L-G, Wang Z, McElwee J, Podtelezhnikov AA, … Emilsson V (2013). Integrated systems approach identifies genetic nodes and networks in late-onset Alzheimer's disease. Cell, 153(3), 707–20. 10.1016/j.cell.2013.03.030 [PubMed: 23622250]

Zhang J, Billingsley ML, Kincaid RL, & Siraganian RP (2000). Phosphorylation of Syk activation loop tyrosines is essential for Syk function. An in vivo study using a specific anti-Syk activation loop phosphotyrosine antibody. Journal of Biological Chemistry, 275(45), 35442–7. 10.1074/jbc.M004549200 [PubMed: 10931839]

Zhao R, Hu W, Tsai J, Li W, & Gan WB (2017). Microglia limit the expansion of β-amyloid plaques in a mouse model of Alzheimer's disease. Molecular Neurodegeneration, 12(1). 10.1186/s13024-017-0188-6

Zumkehr J, Rodriguez-Ortiz CJ, Cheng D, Kieu Z, Wai T, Hawkins C, … Kitazawa M (2015). Ceftriaxone ameliorates tau pathology and cognitive decline via restoration of glial glutamate transporter in a mouse model of Alzheimer's disease. Neurobiology of Aging, 36(7), 2260–2271. 10.1016/j.neurobiolaging.2015.04.005 [PubMed: 25964214]

MAIN POINTS

- Hck inhibition accelerates early stage AD-like pathology by dysregulating microglial function and inducing neuroinflammation.
- Hck plays a prominent role in regulating microglial neuroprotective function during the early stage of AD development.

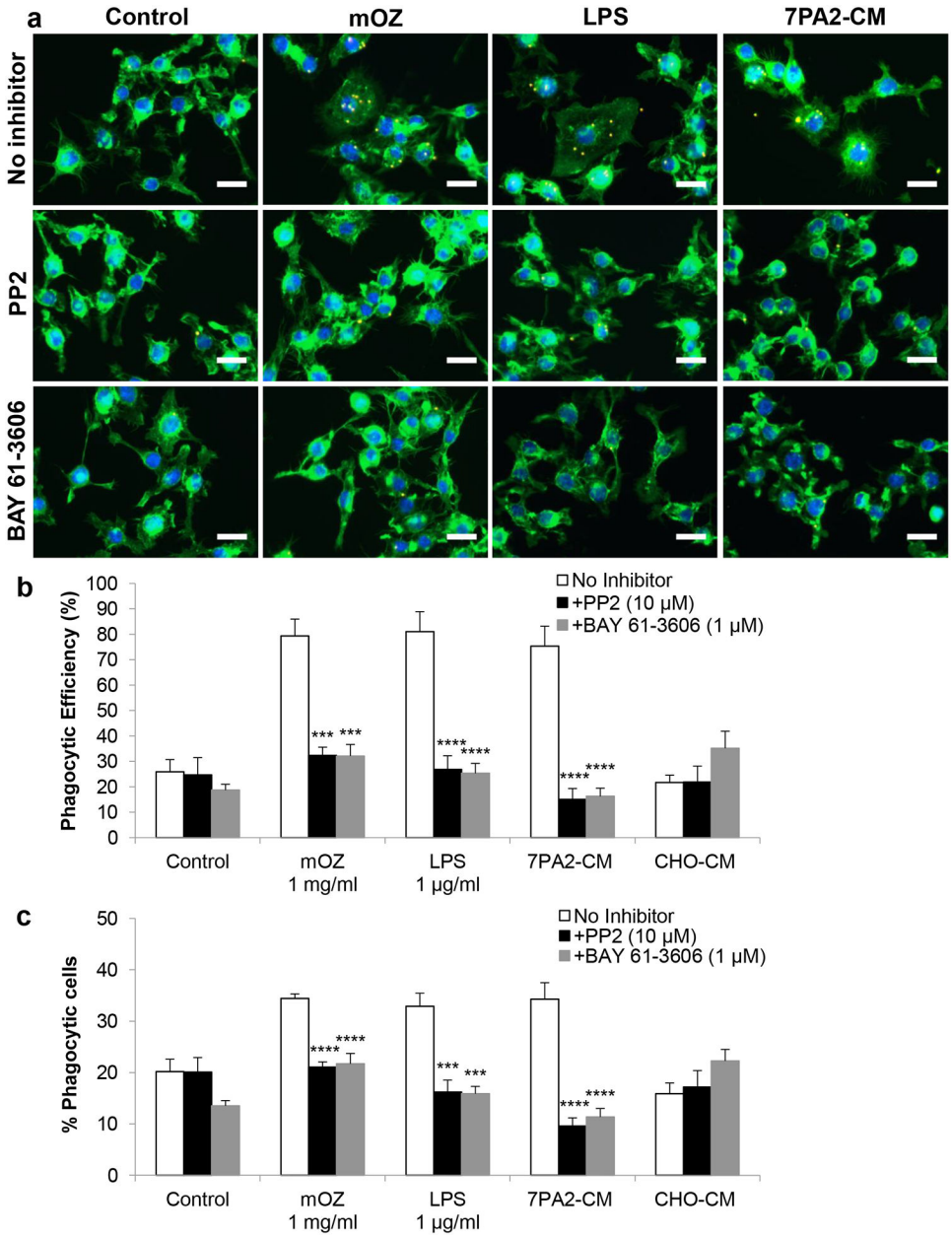

FIGURE 1.

Hck/SFKs and Syk mediated ligands-stimulated activation of phagocytic activity in BV2 murine microglial/macrophage cells. (a) Representative images of BV2 cells after treated with serum free medium (control), mouse-complement opsonized zymosan (mOZ, 1 mg/ml), LPS (1 μg/ml) or naturally secreted Aβ oligomers (AβO) from 7PA2 cells (7PA2-CM), in the presence or absence of pan-Src inhibitor (PP2, 10 μM) or Syk-specific inhibitor (BAY 61–3606, 1 μM). Nile Red microspheres were applied to the cells as markers of phagocytic activity. Cells were labeled with cytoskeleton marker - 488 conjugated Phalloidin in green and nuclei marker - DAPI in blue. Scale bar, 20 μm. (b, c) Number of microspheres phagocytosed by cells under respective conditions were quantified and reported as phagocytic efficiency (%) (b) and % phagocytic cells (c). Phagocytic efficiency (%) accounts

for the weighted average of phagocytosed microspheres per cell. CHO-CM is conditioned medium from CHO cells that was applied as a negative control since 7PA2 cells are derived from CHO cells. Both phagocytic efficiency (%) and % phagocytic cells analyses revealed that BV2 microglial phagocytic activity was stimulated by mOZ, LPS and naturally secreted AβO in 7PA2-CM. However, in the presence of pan-Src (PP2) or Syk (BAY 61–3606) inhibitor, BV2 phagocytic activities were attenuated to that of the basal level, signifying that Hck/SFKs and Syk are responsible for these ligand-stimulated microglial phagocytosis. Data are expressed as mean ± SEM. n = 4–6 from three independent experiments. *** $p < 0.001$ and **** $p < 0.0001$ relative to no inhibitor.

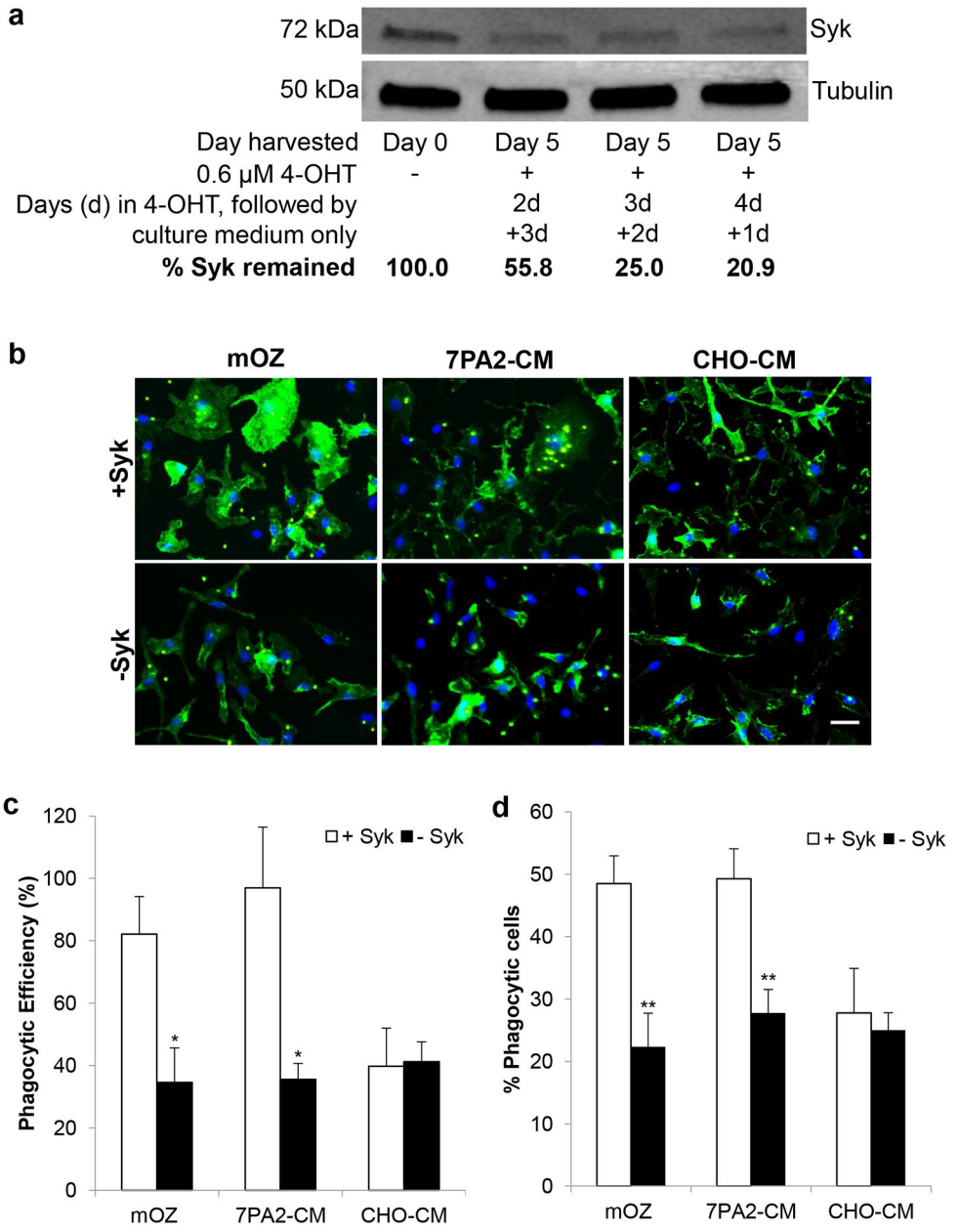

FIGURE 2.

Syk signaling mediated Aβ oligomers (AβO)-stimulated primary microglial phagocytosis. (a) Primary microglia derived from Syk/Cre mice were treated with and without 0.6 μM 4-hydroxytamoxifen (4-OHT) for two to four days (d), followed by culture medium at up to five days to knockdown Syk. Western blot analysis revealed that the steady-state level of Syk was reduced to ~21% at four days 4-OHT and one day (4d+1d) culture medium treatment relative to untreated cells. Tubulin was probed as loading control. (b) Representative images of Syk/Cre primary microglia after treated with mouse-complement opsonized zymosan (mOZ, 1 mg/ml), naturally secreted AβO from 7PA2 cells (7PA2-CM) or conditioned medium from CHO cells (CHO-CM) that serves as a negative control since 7PA2 cells are derived from CHO cells. Syk/Cre primary microglia treated with four days 4-OHT and one

day culture medium are denoted as –Syk, while those untreated are denoted as +Syk. Nile Red microspheres were applied to the cells as markers of phagocytic activity. Cells were labeled with cytoskeleton marker - 488 conjugated Phalloidin in green and nuclei marker - DAPI in blue. Scale bar, 10 μm. (c, d) Both phagocytic efficiency (%) (c) and % phagocytic cells (d) analyses revealed that the phagocytic activity of Syk/Cre primary microglia was stimulated by mOZ or naturally secreted AβO in 7PA2-CM. However, in the absence of Syk, the phagocytic activities of primary microglia were attenuated to that of the basal level as in CHO-CM, signifying that Syk is responsible for these ligand-stimulated microglial phagocytosis. Data are expressed as mean ± SEM. n = 5–7 from four independent experiments. * $p < 0.05$ and ** $p < 0.01$ relative to no Syk knockdown.

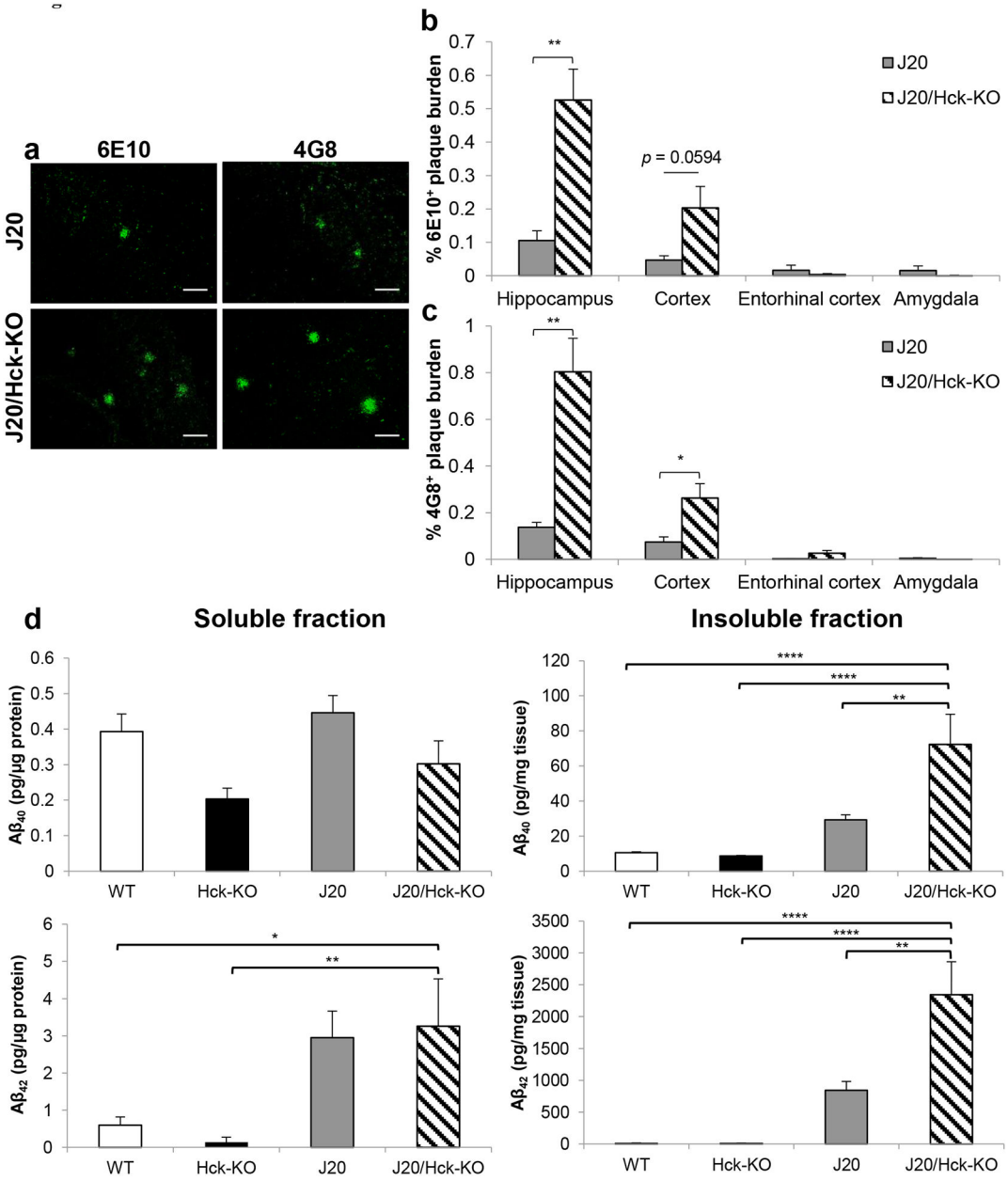

FIGURE 3.

Hck deficiency in J20 mice significantly increased Aβ plaque burden. (a) Representative images of 6E10- (left) and 4G8-positive (right) Aβ plaques found in the hippocampus region of 6–8 months old J20 (n = 8) and J20/Hck-KO (n = 6) mice. Scale bar, 50 µm. (b, c) Quantitative analysis of 6E10- (b) and 4G8-positive (c) Aβ plaques area found in the hippocampus, cortex, entorhinal cortex and amygdala regions of J20 and J20/Hck-KO mice. Significant accumulation of 6E10- and 4G8-positive plaques were observed in the hippocampus and cortex of J20/Hck-KO mice. Data are expressed as mean ± SEM from four sections per mouse. * $p < 0.05$ and ** $p < 0.01$ relative to J20 mice. (d) ELISA quantification of detergent-soluble (left) and -insoluble (right) Aβ40 (top) and Aβ42 (bottom) in protein lysates of mouse hippocampus. Lysates from WT, Hck-KO, J20 and J20/

Hck-KO mice were analyzed at n = 6–8. Significant augmentation of insoluble Aβ40 and Aβ42 were detected when Hck was ablated in J20 mice. * $p < 0.05$, ** $p < 0.01$, and **** $p < 0.0001$ between indicated genotypes.

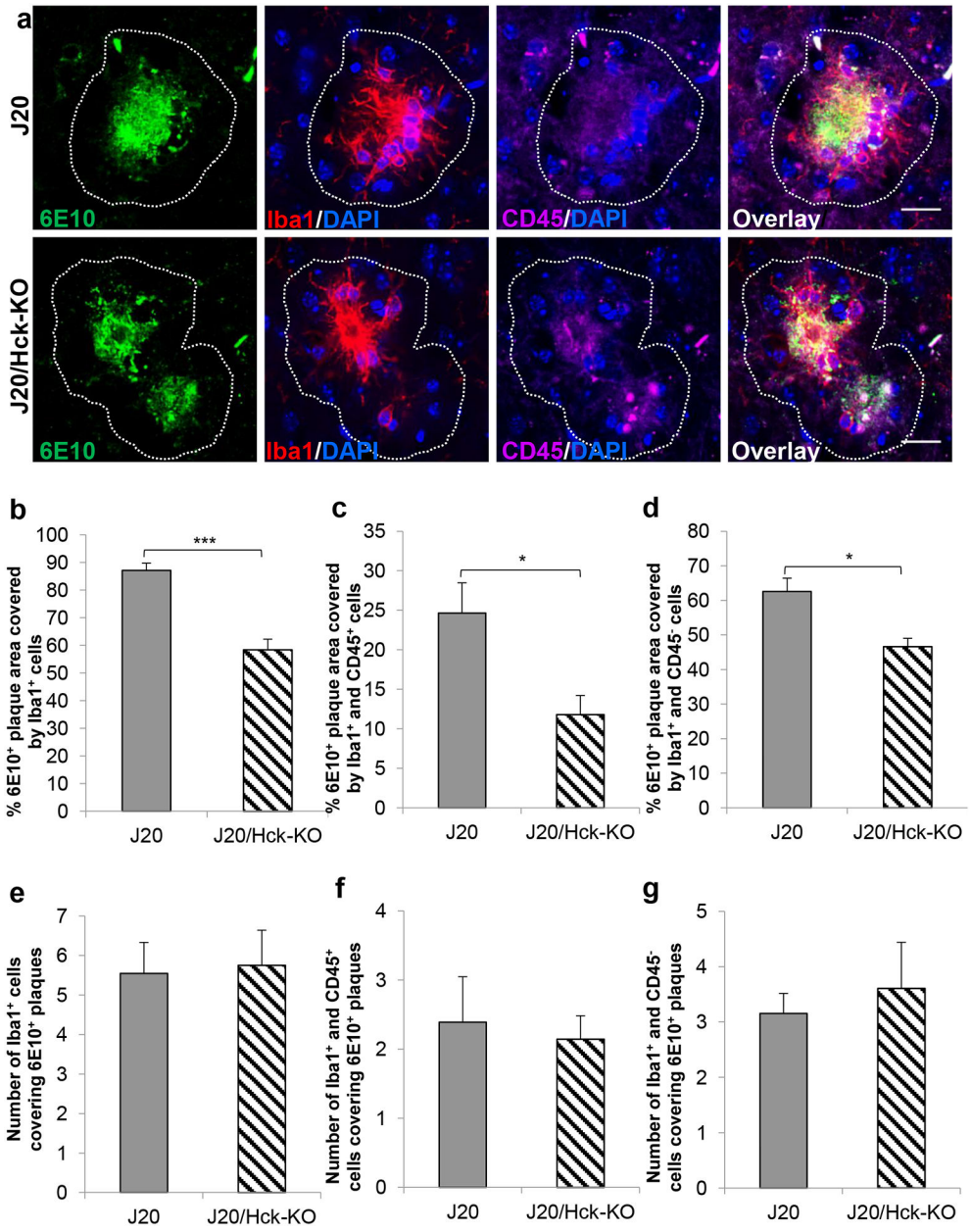

FIGURE 4.

Elimination of Hck in J20 mice significantly reduced microglia coverage on 6E10-positive plaques. (a) Representative images of 6E10-positive plaques (green) clustered by Iba1- (red) and CD45- positive (magenta) microglia/macrophages in J20 (top) and J20/Hck-KO (bottom) mice (6–8 months old). Nuclei stained with DAPI were shown in blue. Dotted line outlines region at 20 μm from the edge of the plaques where plaques and microglia within the region were quantified. Scale bar, 20 μm. (b-d) Quantitative analysis of % 6E10 plaque area covered by $Iba1^+$ (b), $Iba1^+$ and $CD45^+$ (c), or $Iba1^+$ and $CD45^-$ (d) cells revealed significantly lower coverage in J20/Hck-KO mice. (e-g) Number of $Iba1^+$ (e), $Iba1^+$ and $CD45^+$ (f), or $Iba1^+$ and $CD45^-$ (g) cells clustering around 6E10-positive plaques did not show significant difference between the two mouse genotypes. Plaques of ≥ 30 μm were

analyzed in the hemibrains of 6 J20 (n = 19) and 6 J20/Hck-KO mice (n = 31), where there was no significant difference in the distribution of plaque diameter between the two genotypes. Data are expressed as mean ± SEM from three sections per J20 mouse and one section per J20/Hck-KO mouse. * $p < 0.05$ and *** $p < 0.001$ relative to J20 mice.

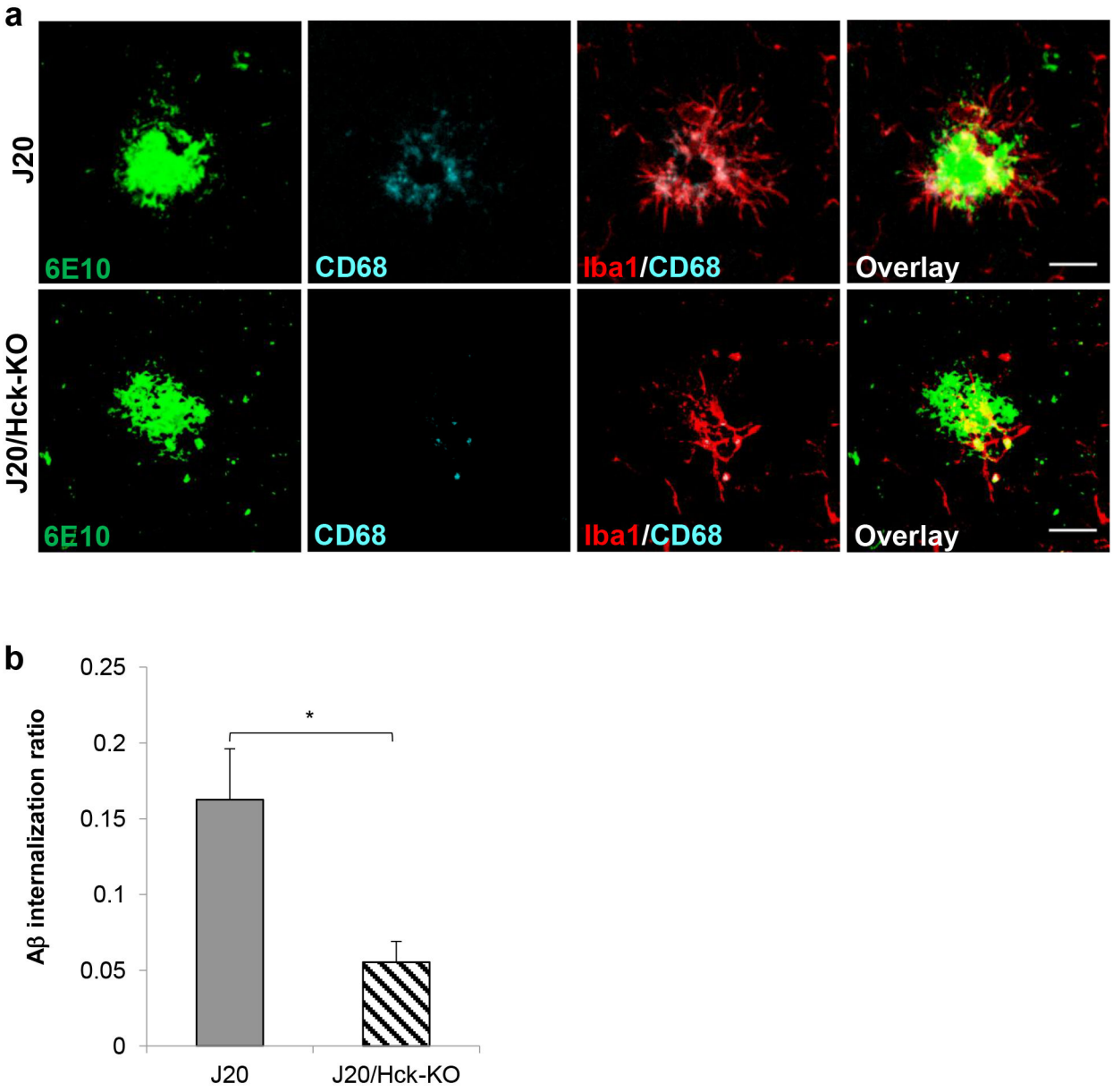

FIGURE 5.

Knocking out Hck in J20 mice significantly reduced Aβ internalization in microglia. (a) Representative images of 6E10-positive plaques (green) clustered by Iba1-positive microglia (red) and CD68-positive microglial phagolysosomes (cyan) in J20 (top) and J20/Hck-KO (bottom) mice (6–8 months old). Scale bar, 20 μm. (b) Quantitative analysis of Aβ internalization ratio revealed a 66% reduction in microglial phagocytic activity in J20/Hck-KO mice. Aβ internalization ratio was calculated by volume of Aβ within microglial phagolysosomes normalized to microglia number on the plaque and Aβ plaque volume in the field. Plaques were analyzed in the hemibrains of 8 J20 (n = 18) and 6 J20/Hck-KO (n = 30) mice. Data are expressed as mean ± SEM from one section per mouse. * $p < 0.05$ relative to J20 mice.

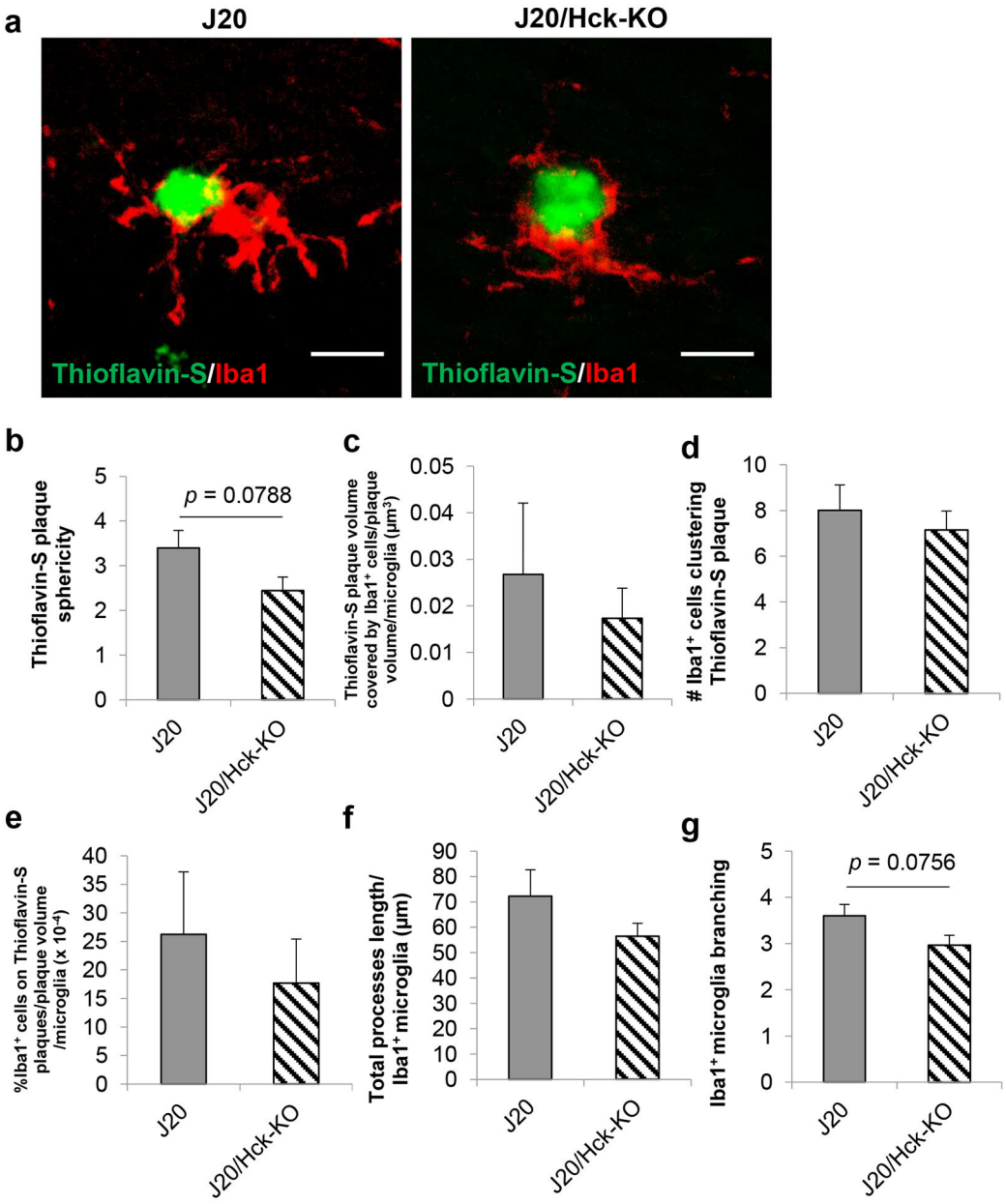

FIGURE 6.

Depleting Hck in J20 mice slightly altered Thioflavin-S sphericity and Iba1$^+$ microglia branching. (a) Representative confocal images of Thioflavin-S plaque (green) clustered by Iba1$^+$ (red) microglia in J20 (left) and J20/Hck-KO (right) mice (6–8 months old). Scale bar, 20 μm. Knocking out Hck reduced, almost significantly, the sphericity of Thioflavin-S plaques when compared to J20 mice (b). Quantification of Thioflavin-S plaque volume covered by Iba1$^+$ cells per plaque volume per cell (c) did not show significant differences between the two mouse genotypes. Volumetric and Imaris automated analyses of Iba1$^+$ cells clustering around Thioflavin-S plaques did not show significant differences in the number of cells (d), % Iba1$^+$ cells clustering Thioflavin-S plaques per plaque volume per cell (e), nor total processes length/Iba1$^+$ microglia (f). Nonetheless, there was near significant reduction

in Iba1^{+} microglia branching in J20/Hck-KO (g). Plaques were analyzed in the hemibrains of 8 J20 (n = 27) and 6 J20/Hck-KO mice (n = 58). Data are expressed as mean ± SEM from one section per mouse.

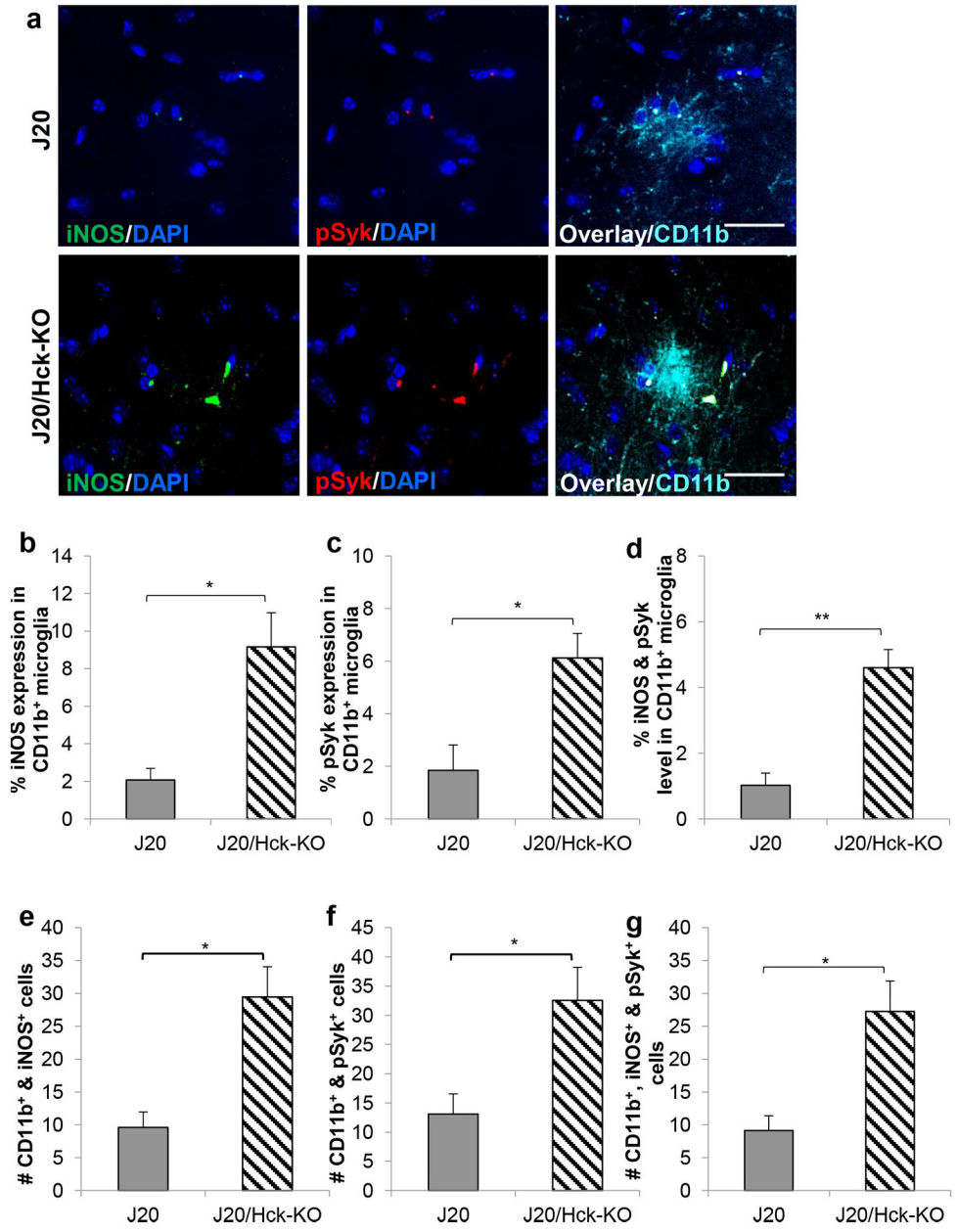

FIGURE 7.

Hck deficiency in J20 mice significantly elevated iNOS and pSyk expression in $CD11b^+$ microglial clusters. (a) Representative images of iNOS (green) and pSyk (red) expressing in $CD11b^+$ (cyan) microglial clusters in J20 (top) and J20/Hck-KO (bottom) mice (6–8 months old). Nuclei stained with DAPI were shown in blue. Scale bar, 20 μm. (b-d) Quantitative analyses of either % iNOS (b), pSyk (c), or both iNOS and pSyk (d) in the $CD11b^+$ microglial clusters showed significantly higher expression in J20 mice depleted of Hck. (e-g) Clusters of microglial cells positively stained for CD11b and iNOS (e), CD11b and pSyk (f), as well as CD11b, iNOS and pSyk (g*)* were also counted. A significantly higher number of cells expressing either $iNOS^+$, $pSyk^+$ or $iNOS^+$ and $pSyk^+$ in $CD11b^+$ cells were observed in J20 mice lacking Hck. Microglial clusters were analyzed in the hemibrains of 4–6 J20 (n =

12–15) and 4–5 J20/Hck-KO mice (n = 8–17). Data are expressed as mean ± SEM from 1–2 sections per mouse. * $p < 0.05$ and ** $p < 0.01$ relative to J20 mice.

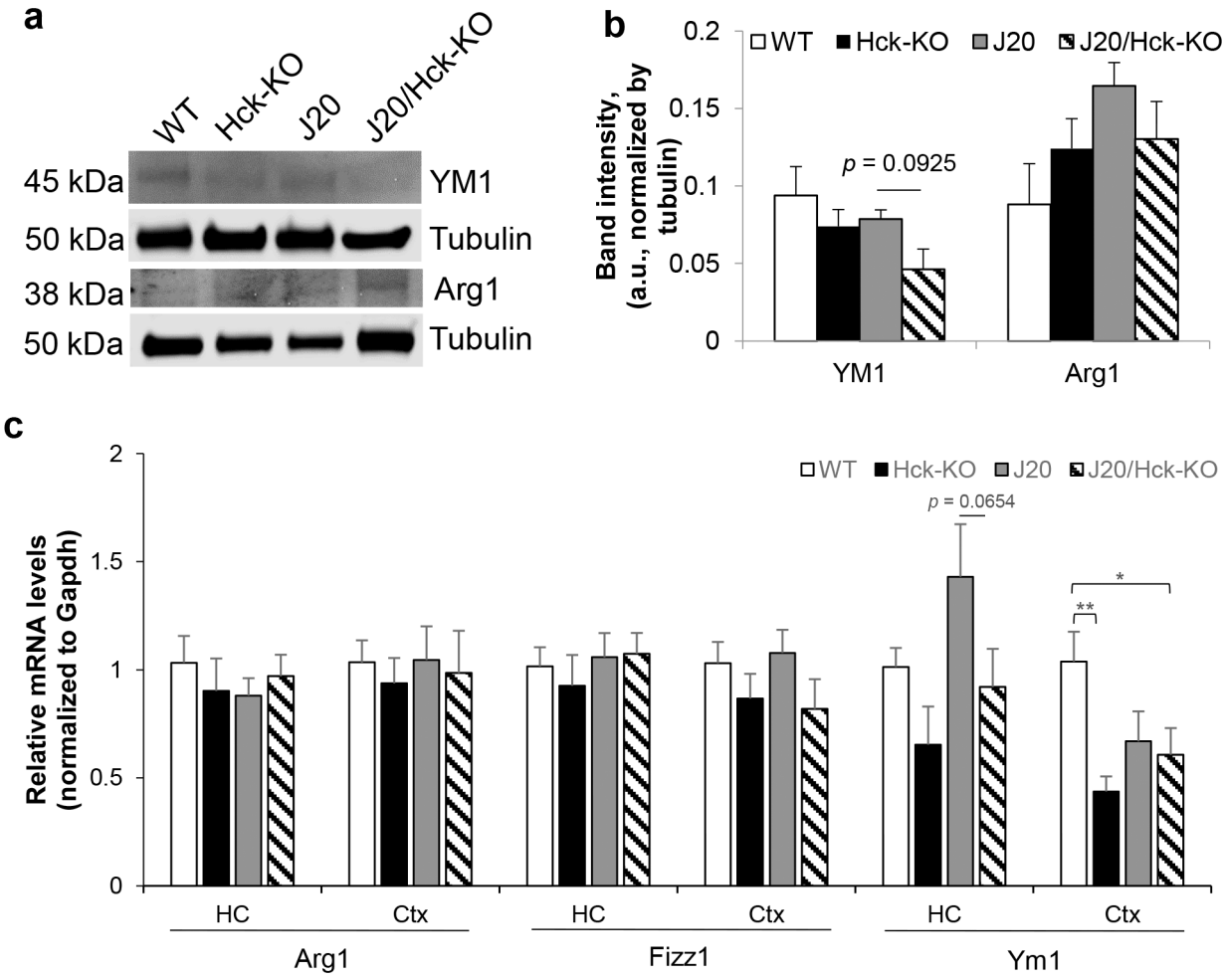

FIGURE 8.

Deleting Hck moderately reduced steady-state and mRNA levels of Ym1 in J20 mice. (a, b) Protein extracts from hippocampal tissues of 6–8 months old WT, Hck-KO, J20 and J20/Hck-KO mice were analyzed by Western blotting. (a) Representative immunoblots of microglial phagocytic markers, YM1 and Arg1, were shown. Tubulin was probed as loading control. (b) Quantitative analysis of YM1 and Arg1 band intensities after normalized to that of tubulin did not show significant differences between genotypes, but there was trend of lower YM1 protein levels in J20/Hck-KO mice as compared to J20 mice. Data are expressed as mean ± SEM from n = 6–8 per genotype. (c) Relative expression of Arg1, Fizz1 and Ym1 mRNA levels were quantified by real-time PCR analyses from the hippocampus (HC) and cortex (Ctx) of WT, Hck-KO, J20 and J20/Hck-KO mice of 6–8 months old. mRNA level of Ym1 was reduced almost significantly ($p = 0.0654$) in the hippocampi of J20/Hck-KO mice as compared to J20 mice. However, significant reduction of Ym1 mRNA level was observed in the cortices of J20/Hck-KO mice as compared to WT mice. Data are expressed as mean ± SEM from n = 3–5 hippocampi and n = 5–8 cortices per genotype. * $p < 0.05$ and ** $p < 0.01$ between indicated genotypes.

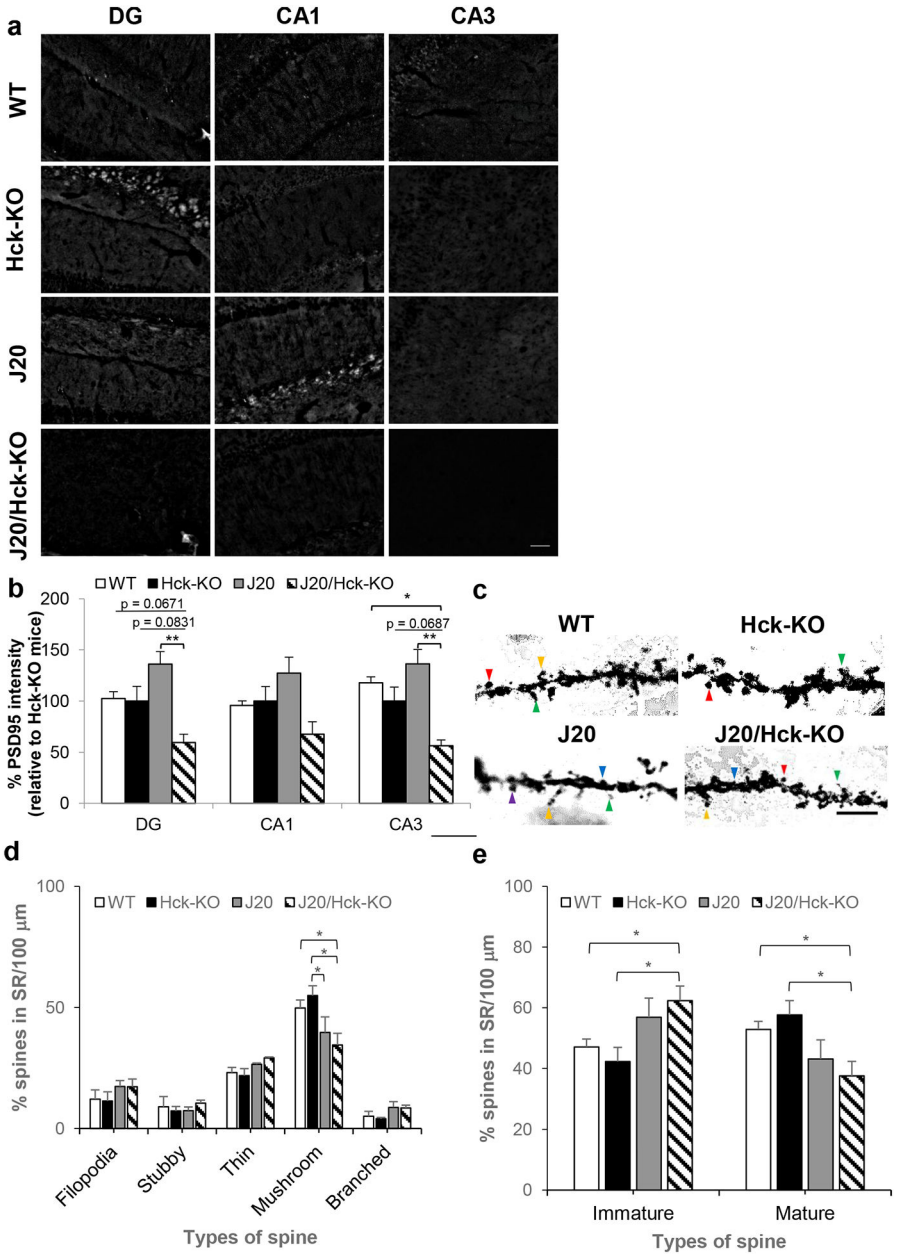

FIGURE 9.

Eliminating Hck in J20 mice significantly reduced intensity of PSD95 in the hippocampal DG and CA3 regions. (a) Representative images of PSD95 (post-synaptic protein marker) at the DG, CA1 and CA3 regions of the hippocampus of WT, Hck-KO, J20 and J20/Hck-KO mice (6–8 months old). Scale bar, 50 µm. (b) Quantitative analyses of % PSD95 intensities in WT, Hck-KO, J20 and J20/Hck-KO mice taken relative to that of Hck-KO mice revealed significant reduction in J20/Hck-KO mice at the DG (compared to J20 mice) and CA3 (compared to WT and J20 mice) regions. Data are expressed as mean ± SEM from one section per mouse with n = 6–8. * $p < 0.05$ and ** $p < 0.01$ between indicated genotypes. (c) Representative images of dendritic spines in 6–8 months old WT, Hck-KO, J20 and J20/Hck-KO mice were shown. Filopodia (yellow arrow), thin (green arrow), stubby (blue

arrow), mushroom (red arrow), and branched (purple arrow) spines were indicated in the images. Scale bar, 5 μm. (d) Quantitative analyses of % filopodia, stubby, thin, mushroom and branched spines in the SR region of hippocampal CA1 per 100 μm dendrite analyzed revealed significant reduction of mushroom spine in J20/Hck-KO mice relative to WT or Hck-KO mice. (e) A replot of the data by expressing % immature (sum of filopodia, stubby and thin spines relative to total spine) and % mature (sum of mushroom and branched spines relative to total spine) spines showed more immature spine but fewer mature spine in J20/Hck-KO mice as compared to WT or Hck-KO mice. Data are expressed as mean ± SEM from 4 mice per genotype where 25–35 pyramidal neurons were analyzed for each mouse. * $p < 0.05$ relative to WT or Hck-KO mice.

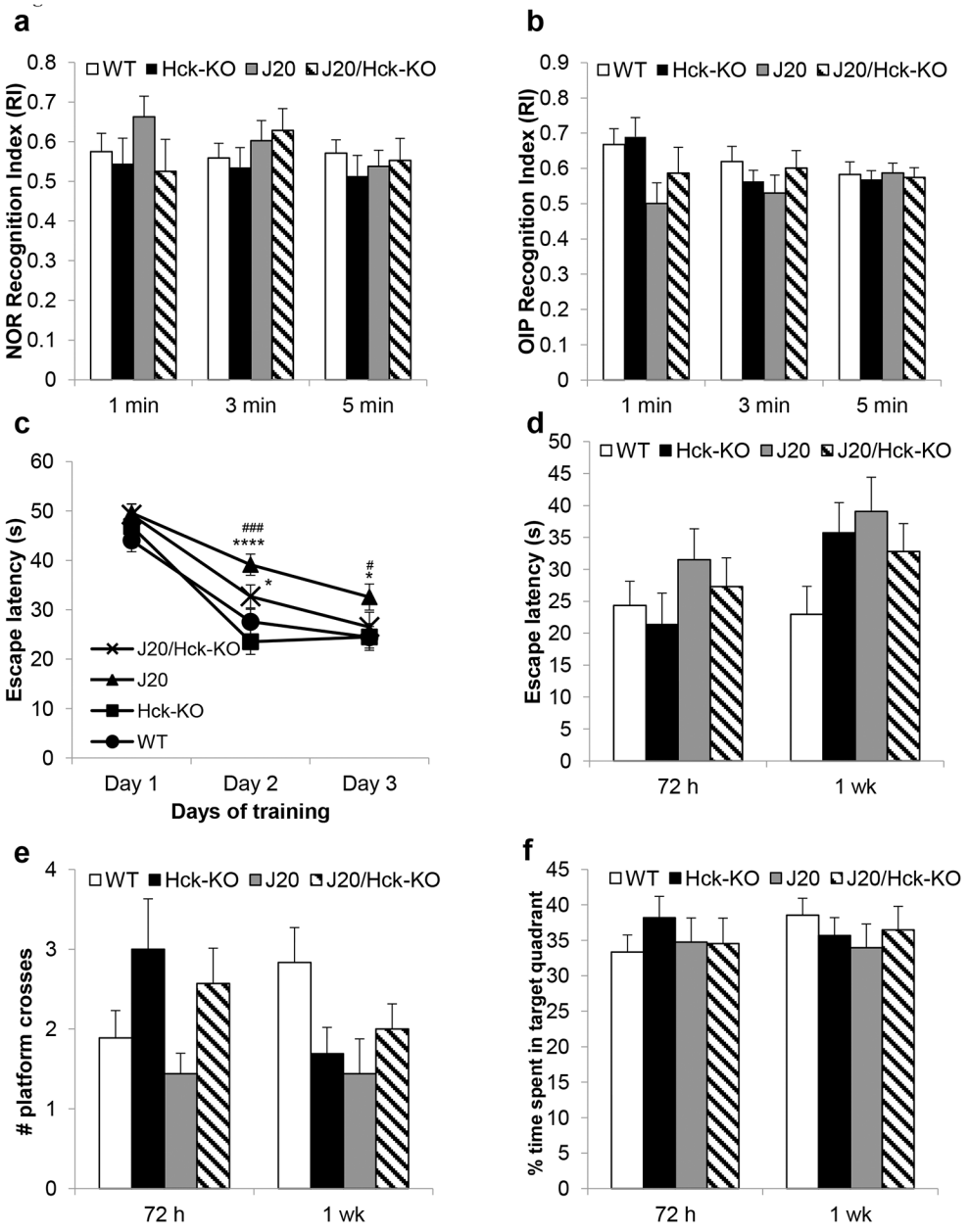

FIGURE 10.

Knocking out Hck did not modulate cognitive phenotypes in J20 mice. (a-f) WT, Hck-KO, J20 and J20/Hck-KO mice of 5–6 months were subjected to a battery of behavioral tests, namely NOR (a), OIP (b) and MWM (c-f). There were no significant differences in the recognition index (RI) of NOR (a) and OIP (b) tests between the genotypes during the 1, 3 and 5 mins of the experiments. MWM training revealed that J20/Hck-KO mice took significantly longer escape latency than Hck-KO mice on the second day of training, but had comparable latency with WT and Hck-KO mice on the third day (c). n = 13–18, * $p < 0.05$ and **** $p < 0.0001$ relative to Hck-KO mice; $^{\#}$ $p < 0.05$ and $^{\#\#\#}$ $p < 0.001$ relative to WT mice (Repeated measures two-way ANOVA with multiple comparisons of performance by genotype per day). At 72 h and 1 wk after last MWM training, J20/Hck-KO showed trend of

shorter but not significant escape latency than J20 mice in both MWM tests (d). The data coincided with slightly more crosses observed in J20/Hck-KO mice than J20 mice during the 72 h and 1 wk tests (e). There was no significant difference in the % time spent in the target (f) quadrant between the genotypes either. Data are expressed as mean ± SEM at n = 13–18.